Ore Geology Reviews 75 (2016) 304–326

Contents lists available at ScienceDirect

Ore Geology Reviews

journal homepage: www.elsevier.com/locate/oregeorev

Alteration and mineralization at the Zhibula Cu skarn deposit, Gangdese belt, Tibet

Jing Xu [a], Youye Zheng [a,b,*], Xiang Sun [b,**], Yahui Shen [b]

[a] State Key Laboratory of Geological Processes and Mineral Resources, and Faculty of Earth Resources, China University of Geosciences, Wuhan 430074, China
[b] State Key Laboratory of Geological Processes and Mineral Resources, and School of Earth Science and Resources, China University of Geosciences, Beijing 100083, China

ARTICLE INFO

Article history:
Received 30 June 2015
Received in revised form 21 November 2015
Accepted 24 November 2015
Available online 2 December 2015

Keywords:
Zonation
Stable isotope
Fluid inclusion
Cu skarn
Zhibula
Tibet

ABSTRACT

The Zhibula Cu skarn deposit contains 0.32 Mt. Cu metal with an average grade of 1.64% and is located in the Gangdese porphyry copper belt in southern Tibet. The deposit is a typical metasomatic skarn that is related to the interaction of magmatic–hydrothermal fluids and calcareous host rock. Stratiform skarn orebodies occur at the contact between tuff and marble in the Lower Jurassic Yeba Formation. Alteration zones generally grade from a fresh tuff to a garnet-bearing tuff, a garnet pyroxene skarn, and finally to a wollastonite marble. Minor endoskarn alteration zonations are also observed in the causative intrusion, which grade from a fresh granodiorite to a weakly chlorite-altered granodiorite, a green diopside-bearing granodiorite, and to a dark red-brown garnet-bearing granodiorite. Prograde minerals, which were identified by electron probe microanalysis include andradite–grossularite of various colors (e.g., red, green, and yellow) and green diopside. Retrograde metamorphic minerals overprint the prograde skarn, and are mainly composed of epidote, quartz, and chlorite. The ore minerals consist of chalcopyrite and bornite, followed by magnetite, molybdenite, pyrite, pyrrhotite, galena, and sphalerite. Three types of fluid inclusions are recognized in the Zhibula deposit, including liquid-rich two-phase inclusions (type L), vapor-rich two-phase inclusions (type V), and daughter mineral-bearing three-phase inclusions (type S). As the skarn formation evolved from prograde (stage I) to early retrograde (stage II) and later retrograde (stage III), the ore-forming fluids correspondingly evolved from high temperature (405–667 °C), high salinity (up to 44.0 wt.% NaCl equiv.), and high pressure (500–600 bar) to low-moderate temperature (194–420 °C), moderate-high salinity (10.1–18.3 and 30.0–44.2 wt.% NaCl equiv.), and low-moderate pressure (250–350 bar). Isotopic data of $\delta^{34}S$ (−0.1‰ to −6.8‰, estimated $\delta^{34}S_{fluids}$ = −0.7‰), δD_{H2O} (−91‰ to −159‰), and $\delta^{18}O_{H2O}$ (1.5‰ to 9.2‰) suggest that the ore-forming fluid and material came from magmatic–hydrothermal fluids that were associated with Miocene Zhibula intrusions. Fluid immiscibility likely occurred at the stage I and stage II during the formation of the skarn and mineralization. Fluid boiling occurred during the stage III, which is the most important Cu deposition mechanism for the Zhibula deposit.

1. Introduction

The word ‘skarn’ in its present-day sense was first published by Törnebohm (1875) and was defined as peculiar, dark ore hosting rock and subordinate layer in feldspar-poor felsic volcanic rock. Subsequently, skarn dominated by calc-silicate mineral assemblages, such as garnet and pyroxene, is known as a relatively simple rock type that is defined by its mineralogy and generally occurs along the contact between intrusion and carbonate rock (Einaudi et al., 1981; Meinert et al., 1997). The genesis of skarn and related deposits is mostly due to contact metasomatism that are associated with magmatic–hydrothermal fluids, whereas some scholars suggested that these strata-bound skarns are associated with the hydrothermal metasomatism of previous source beds (Chang and Liu, 1983), magmatic skarn that crystallized from immiscible iron-copper oxide melt (Wu, 1992), and sedimentary exhalative skarn that is related to exhalative sedimentation (Lu et al., 1999; Yokoro et al., 2013). Skarn is the most crucial ore hosting rock in skarn-related ore systems, and the mineral species, composition, distribution, and formation play critical roles in constraining its genesis (Smith et al., 2004; Calagari and Hosseinzadeh, 2006; Canet et al., 2011; Zhang et al., 2013). Most skarn ore systems are zoned, namely, proximal garnet, distal pyroxene, and wollastonite near the marble front (Meinert et al., 2005). Moreover, the proximal garnet, distal garnet, and garnet near the marble front are generally dark red-brown, pale brown, and pale yellow-green, respectively (Atkinson and Einaudi, 1978). The Fe and Mn contents in pyroxene gradually increase with greater proximity to marble (Harris and Einaudi, 1982). Einaudi et al. (1981) proposed that the paragenetic assemblage of andradite and

* Corresponding author at: State Key Laboratory of Geological Processes and Mineral Resources, and Faculty of Earth Resources, China University of Geosciences, Wuhan 430074, China.
** Corresponding author.
E-mail addresses: zhyouye@163.com (Y. Zheng), sunxiang@cugb.edu.cn (X. Sun).

http://dx.doi.org/10.1016/j.oregeorev.2015.11.028
0169-1368/

diopside indicate that the formation environment had low acidity and high oxygen fugacity. Most garnet crystals exhibit obvious oscillatory zonings that record the circulation and stagnation of fluid (Jamtveit, 1991).

The origins of ore-forming materials vary in different deposits because of various controls on ore forming processes, such as the lithology (including the chemical and physical properties of the host rocks, the composition and the depth of intrusive rock), tectonics, etc. Most researchers investigated that metallogenic materials were derived from magma (Ault, 2004; Shu et al., 2013; Zhai et al., 2014), and some scholars considered mixed sources from intrusive and sedimentary rocks (Ishihara et al., 2000; Zeng et al., 2009; Yokoro et al., 2013). However, few studies suggested that these materials came only from wall rocks ($\delta^{34}S$ ranges from 10.8‰ to 26.5‰, which is consistent with the values of seawater, and the Pb isotope ratios in the ores are unrelated to those in the granite; Gemmell et al., 1992). Several studies have observed that the formation of both anhydrous and hydrous assemblages involved only magmatic water (Meinert et al., 2003; Baker et al., 2004; Bertelli et al., 2009; Williams-Jones et al., 2010; Mei et al., 2014). Ore-forming fluids that were obtained from fluid inclusions indicate that they are magmatic–hydrothermal with high temperature, high salinity, and abundant CO_2 (Chen et al., 2007; Kamvong and Zaw, 2009). Meinert et al. (1997) investigated the Big Gossan Cu–Au deposit and concluded that both the high- and low-temperature fluids can be modeled as originating from the exsolution of an underlying intrusion and that the variations in the fluid at different stages resulted from different fluid exsolution times and varying cooling paths (e.g., temperature and pressure). Undoubtedly, fluid boiling is a significant mechanism for metal precipitation (Baker and Lang, 2003; Chen et al., 2007; Samson et al., 2008; Zhu et al., 2012). By contrast, some investigations indicated that even though skarn probably was produced by magmatic fluids, mineralization was generated by fluid mixing between magmatic water and meteoric water, which played an increasing role toward the end of ore precipitation (Einaudi et al., 1981; Singoyi and Zaw, 2001; Lu et al., 2003; Fan et al., 2004; Kamvong and Zaw, 2009; Koděra et al., 2010; Soloviev et al., 2013).

The Zhibula Cu skarn deposit has been investigated by some researchers, including metallogenic epochs (16.9 ± 0.64 Ma, Li et al., 2005), intrusion dating (16.0 ± 0.4 Ma, Yao et al., 2015), and skarn characteristics (Xiao et al., 2011; Xu et al., 2014). However, a systematic study on ore-forming fluids and metallogenic materials has not yet been performed. This paper systematically investigates the alteration and mineralization of the local geology, the mineral components with electron probe microanalysis, the fluid inclusions with microthermometry and laser Raman spectroscopy, and H–O–S stable isotopes. We provide constraints on the source of the ore-forming material and fluid, discuss the metallogenic evolution process, and finally establish a metallogenic model.

2. Regional geology

The Indian–Asian collision and continuous northward movement of the Indian continent created the Himalayan-Tibetan plateau, which has the thickest crust on Earth (Fig. 1a; Yin and Harrison, 2000). The Himalayan-Tibetan plateau primarily contains four continental blocks that include, from south to north, the Himalaya, Lhasa, Qiangtang, and Songpan-Ganzi terranes, which are separated by the Indus-Yarlung Zangbo suture zone (IYZSZ), Jinsha suture zone (JSSZ), and Bangong-Nujiang suture zone (BNSZ) (Fig. 1b). The Lhasa block is divided into the northern Gangdese (NG), central Gangdese (CG), Gangdese back-arc fault uplift belt (GBAFUB), and southern Gangdese (SG), which are separated by the Shiquan River-Nam Tso Mélange Zone (SNMZ), Gar-Lunggar-Zhari Nam Tso-Comai Fault (GLZCF) and Shamolei-Maila-Luobadui-Milashan Fault (SMLMF) (Fig. 1c). The Gangdese porphyry copper belt that is discussed in the paper, is located to the east of the 1000 km-long Gangdese tectonic-magmatic belt in SG, and has experienced a complex tectonic history from the Early Jurassic subduction of the Neo-Tethyan ocean to the Cenozoic India–Asian continental

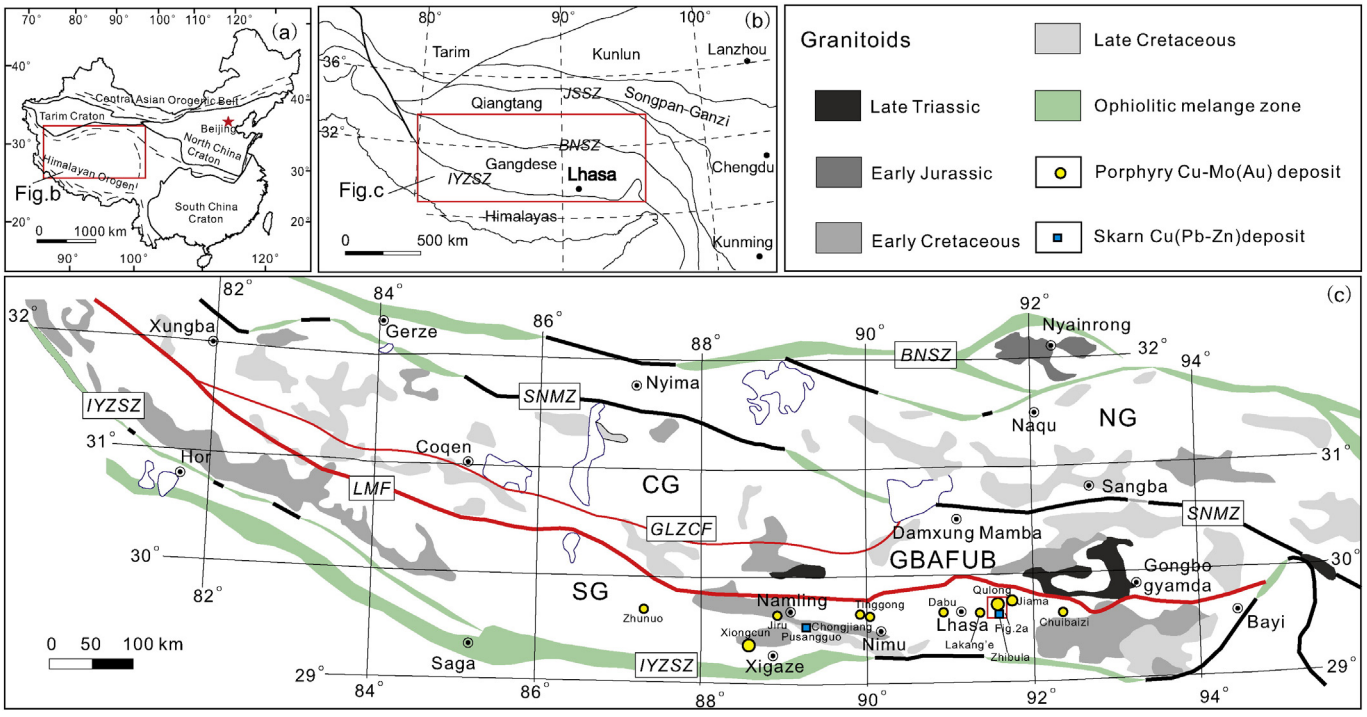

Fig. 1. (a) Simplified structural map of China. (b) Tectonic framework of the Himalayan-Tibetan plateau. (c) Simplified geologic map of the Lhasa block showing the major tectonic subdivisions, distribution of main deposits, and position of the study area (modified after Zheng et al., 2014). Abbreviations: JSSZ = Jinsha Suture Zone, BNSZ = Bangong-Nujiang Suture Zone, SNMZ = Shiquan River-Nam Tso Mélange Zone, GLZCF = Gar-Lunggar-ZhariNam Tso-Comai Fault, LMF = Luobadui-Milashan Fault, IYZSZ = Indus-Yarlung Zangbo Suture Zone, SG = Southern Gangdese, CG = Central Gangdese, GBAFUB = Gangdese Back-Arc Fault Uplift Belt, and NG = Northern Gangdese.

collision and post collision (Yin and Harrison, 2000; Chung et al., 2003; Deng et al., 2014; Hou et al., 2011; Zheng et al., 2014, 2015). The magmatism in SG can be generally divided into four phases, including the Lower Jurassic arc volcanic rocks and arc granites of the Yeba Formation, granites that are related to Late Cretaceous subduction, volcanic rocks from the Linzizong Group and coeval collision-type granites that date from the Paleocene to the Eocene, and porphyries and granites that are associated with large-scale porphyry Cu deposits from the Oligocene and Miocene (Geng et al., 2005; Zheng et al., 2004, 2014; Sun et al., 2013, 2016; Wu et al., 2016). The Gangdese porphyry copper belt is the largest copper belt in China that has been found thus far, where more than 10 large and super-large ore deposits have been discovered, including the Qulong porphyry Cu–Mo deposit (approximately 10 Mt. of Cu and 0.44 Mt. of Mo metal; Zheng et al., 2013), the Zhunuo porphyry Cu–Mo–(Au) deposit (approximately 2.3 Mt. of Cu metal; Zheng et al., 2015), and the Jiama porphyry — skarn Cu–Mo–Au–Ag–Pb–Zn deposit (approximately 5 Mt. of Cu, 0.55 Mt. of Mo, 105 t of Au, 7000 t of Ag, and 0.56 Mt. of Pb + Zn metal; Tang et al., 2011) (Fig. 1c).

3. Geology of the ore deposit

The Zhibula Cu skarn deposit is located approximately 2 km south of the Qulong porphyry Cu–Mo deposit (Fig. 2a) and constitutes a porphyry–skarn metallogenic system along with the Qulong deposit (Li et al., 2005; Xiao et al., 2011). The Lower Jurassic Yeba Formation, which predominantly comprises tuff that has partly metamorphosed to (pyroxene) hornfels and mixed with a small amount of marble and meta-quartz sandstone, is the major lithostratigraphic unit (Xiao et al., 2011). The formation strikes west-northwest with a dip of 70° to 90° and are consistent with the regional structures (Fig. 2b,c). Thrust faults (F1, F2, F3, and F8) lie in this area and control the distribution of the orebodies, which developed in fracture breccias, cataclastic rocks, and fault gouges with skarn and mineralization, such as garnet, magnetite, and minor chalcopyrite. The F2 fault is distributed in the center of the mining area, and strikes west-northwest with a dip of 85°. The northwest trending and subparallel F4, F5, F6, and F7 faults and the northeast-trending F9 fault formed after the orebodies. As shown in Fig. 2a, large intrusions are not observed and no outcrops are evident in the mine, except for some granodiorites and monzogranites that are observed deep in drill holes, such as from 414.5 to 421.5 m and from 450.8 m to the end of the drill hole ZK2007, from 425 to 432 m of the drill hole ZK2014, and from 329.4 to 330 m and from 362 m to the end of the drill hole ZK2407. The granitoid has limited thickness and intruded into the tuff, so we speculate that the intrusion formed dikes or apophyses. Precise in situ SIMS zircon U–Pb ages revealed that the Zhibula granodiorite and monzogranite, which formed at

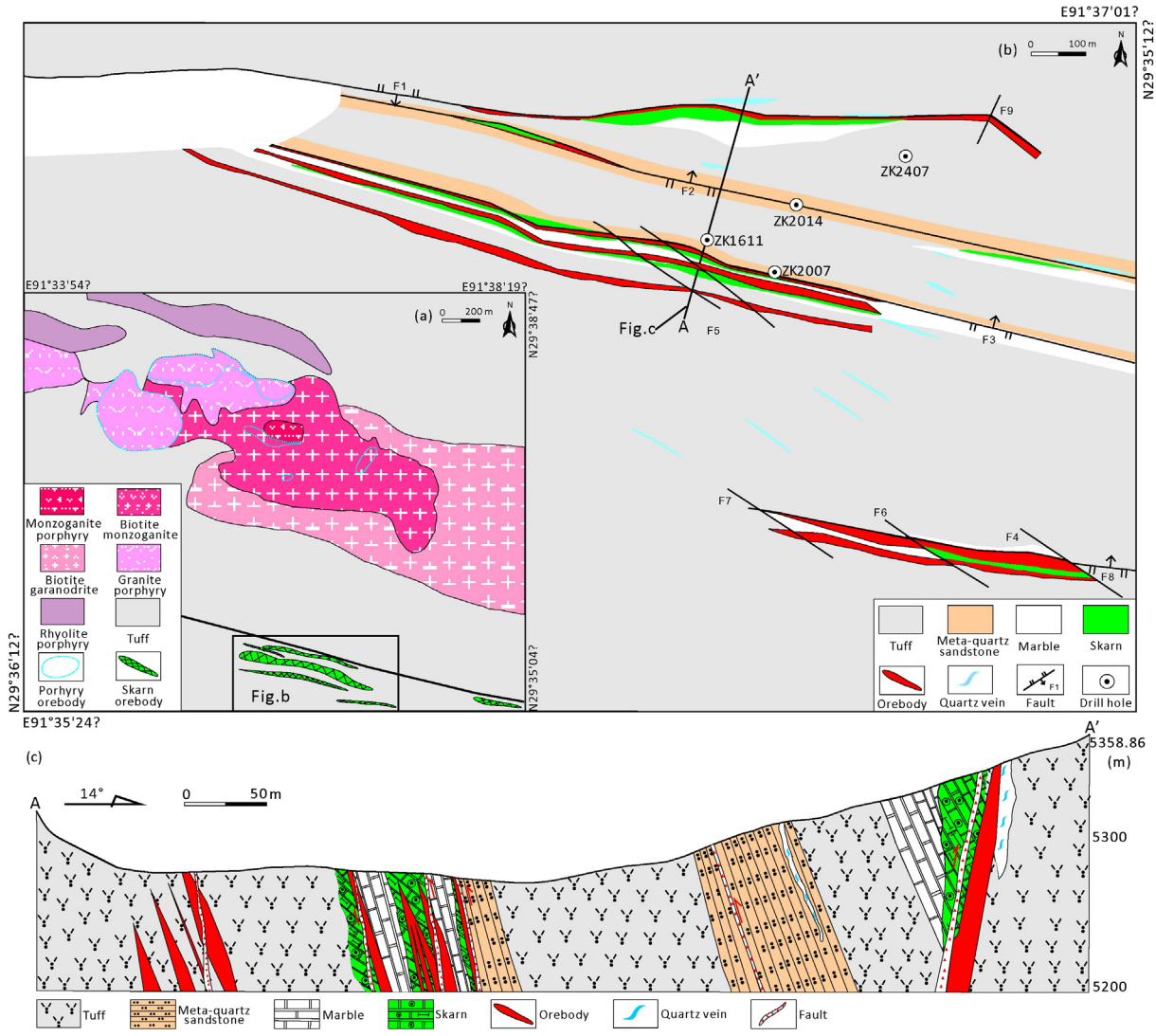

Fig. 2. (a) Regional geological map of the Qulong ore district including the Zhibula deposit (modified after Zheng et al., 2004). (b) Geological map of the Zhibula Cu skarn deposit. (c) Geological cross section A — A' (No.16 exploration line).

approximately 17 Ma (unpublished data), are consistent with the Re–Os isochron age of molybdenite (16.9 ± 0.64 Ma, Li et al., 2005) and are associated with Cu skarn mineralization.

Endoskarn is locally observed in granodiorite close to the contact areas and consists of an assemblage of garnet ± diopside ± chlorite. The granodiorite, which is light gray and coarse- to medium-grained, is principally composed of plagioclase (40–45 vol.%), quartz (20–25 vol.%), and K-feldspar (15–20 vol.%), followed by biotite (10–15 vol.%) and hornblende (5–10 vol.%). Accessory minerals, including sphene, zircon, magnetite, and apatite, occur as inclusions within the essential minerals (Fig. 3a,b). Endoskarn is generally zoned from a dark red-brown garnet at the skarn-intrusive contact to a green diopside-bearing granodiorite, a slight chlorite-altered granodiorite, and a fresh granodiorite (Fig. 4, at depths of 432 to 420.5 m in the drill hole ZK2014). The garnet endoskarn mainly consists of dark red-brown garnet, plagioclase, and bits of diopside (Fig. 3c,d). Diopside endoskarn is primary composed of diopside, quartz, and plagioclase, followed by sphene, apatite, and epidote (Fig. 3e,f).

Similarly to the endoskarn in the granodiorite, exoskarn also reflects a certain order of zonation. As shown in the drill hole ZK1611 (Fig. 5), skarn and mineralization can be divided into several layers. These zones generally grade from a fresh tuff to a garnet-bearing tuff, a garnet skarn (changing from dark garnet to pale garnet), a pyroxene skarn, and finally a wollastonite-bearing marble. This zonation is similar to the conclusion by Atkinson and Einaudi (1978), who stated that intrusions or heat sources change skarn zonations from proximal garnet skarn to distal pyroxene skarn and that proximal garnets are generally dark red-brown, whereas distal garnets near the marble are generally yellow-green. However, the tuff is not related to the Cu skarn mineralization because it formed during the Early Jurassic, which significantly differs from the mineralization age of the Miocene (Li et al., 2005). Skarns, particularly the dark red-brown garnet skarn, are closely spatially associated with mineralization and contain ore minerals, such as chalcopyrite, bornite, and magnetite. Only trace chalcopyrite and bornite was observed in the granodiorite that is associated with typical garnet and diopside endoskarn (Fig. 4).

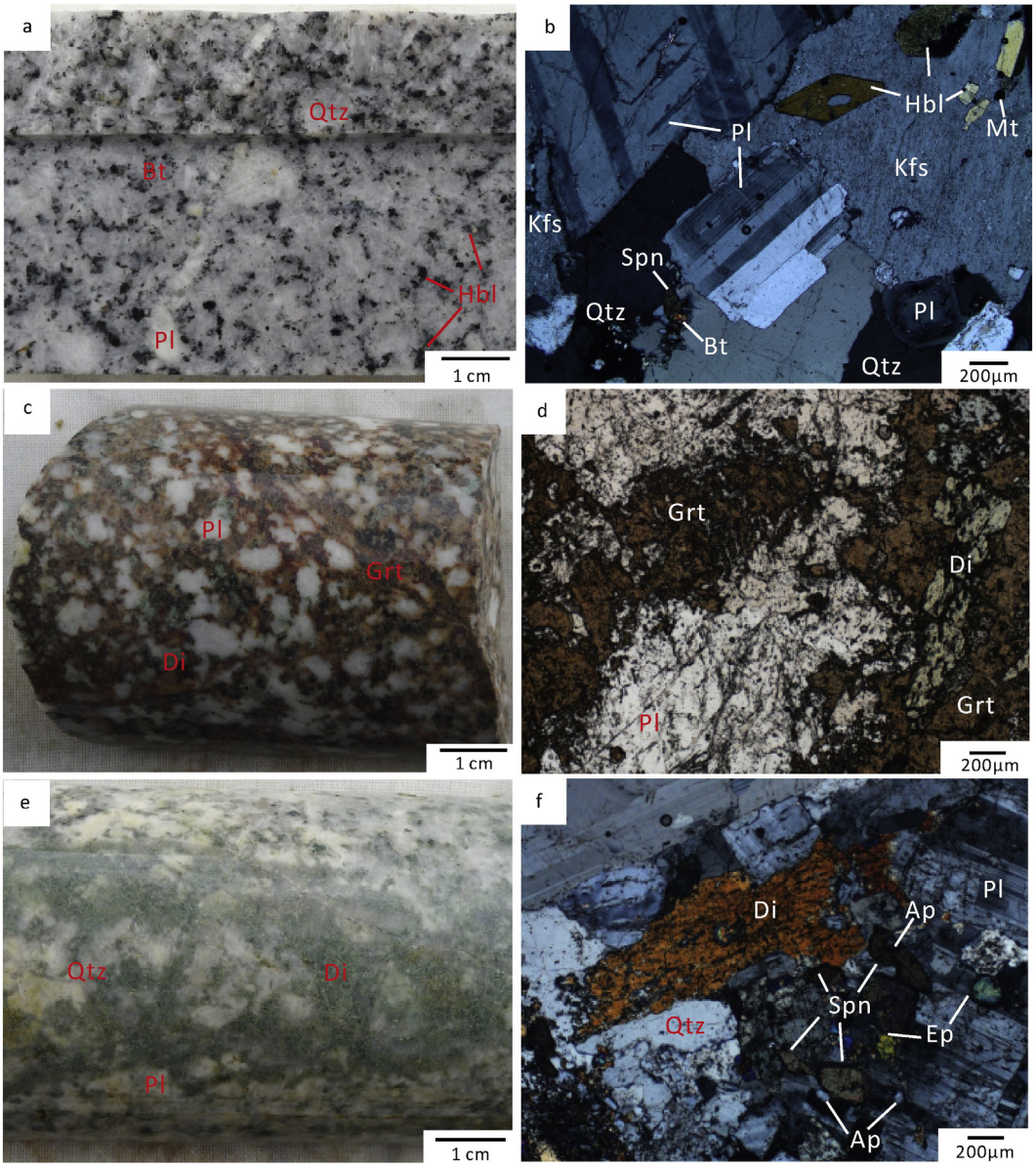

Fig. 3. Representative hand specimen photographs (a, c, and e) and photomicrographs (b, d, and f) of drill core samples from the Zhibula deposit. (a–b) Photograph of granodiorite. The plagioclases have twins and minor oscillatory zoning. (c–d) Dark red-brown garnet skarn in endoskarn with minor diopsides. (e–f) Green diopside skarn in endoskarn without garnets. Mineral symbols: Qtz, Quartz; Kfs, K-feldspar; Pl, Plagioclase; Hbl, Hornblende; Bt, Biotite; Spn, Sphene; Ap, Apatite; Mt., Magnetite; Di, Diopside; Grt, Garnet; Ep, Epidote.

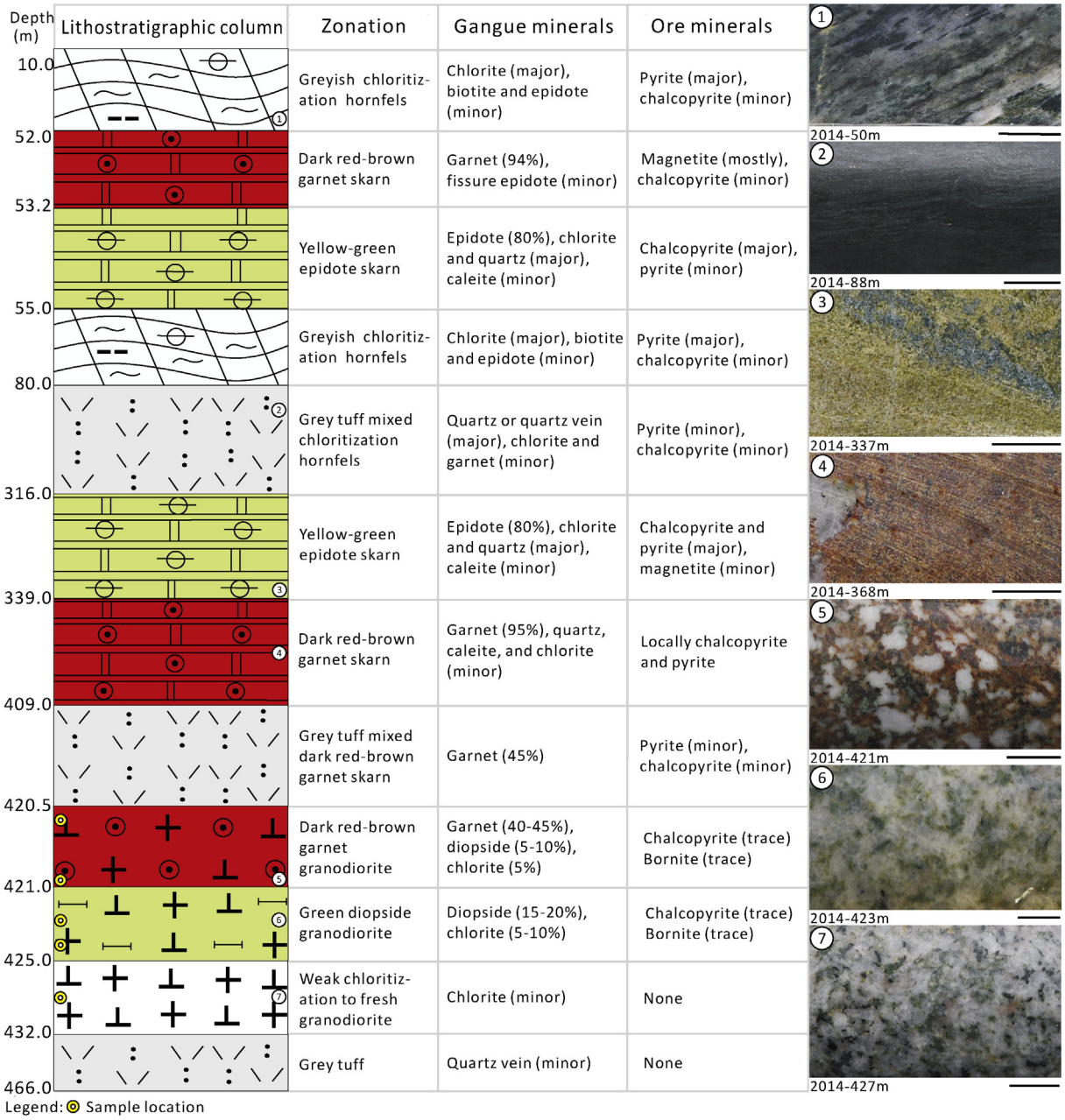

Fig. 4. Lithostratigraphic column and zonation of skarn in drill hole ZK2014. The last column includes representative hand specimen photographs for different drill hole depths. The scale bars in all the photographs are one centimeter in length.

Four orebodies are primarily hosted in interbeds between the tuff and marble in the Yeba Formation; these layers are less lenticular and parts of the orebodies are controlled by fractures in the tuff. The orebodies contain 19.5 Mt. of 1.64% Cu (0.32 Mt. of Cu metal) (Li et al., 2012, Julong Copper Co., LTD). The ore minerals mostly consist of chalcopyrite and bornite, followed by magnetite, molybdenite, pyrite, galena, sphalerite, and pyrrhotite, along with minor chalcocite, hematite, and arsenopyrite. Gangue minerals are commonly composed of garnet and diopside, followed by epidote, wollastonite, calcite, and quartz, and a small amount of tremolite, actinolite, chlorite, and sericite. Based on field geology observations, hand specimens, and petrography, the Zhibula Cu skarn mineralization is similar to typical metasomatic skarn deposits that are related to magmatic-hydrothermal fluids, which develop through a prograde stage (stage I), to an early retrograde stage (stage II), and a late retrograde stage (stage III) (Meinert et al., 2005). During stage I, garnet was the main anhydrous silicate mineral (Fig. 6a-b). Pyroxene and minor wollastonite mainly occurred at the contacts between off-white marble and garnet skarn. These skarns were principally dense with massive texture, while minor amounts were distributed in the wall rock in veins or veinlets, and were partly cut off and replaced by late minerals (Fig. 6a-b). Later in this stage, abundant disseminated and massive magnetite formed by the alteration of prograde anhydrous silicate minerals, particularly garnet. Minor contemporary hematite was also produced by replacing magnetite (Fig. 6a-c,g). Epidote, tremolite, and actinolite that formed by replacing early garnet, pyroxene, and magnetite were the main hydrous silicate minerals during the stage II (Fig. 6b,d). The retrograde skarn contents was less than that of prograde skarn. Abundant chalcopyrite, bornite, quartz, and calcite, followed by pyrite, pyrrhotite, molybdenite, galena, and sphalerite, occurred during stage III (Fig. 6f-k). These minerals were

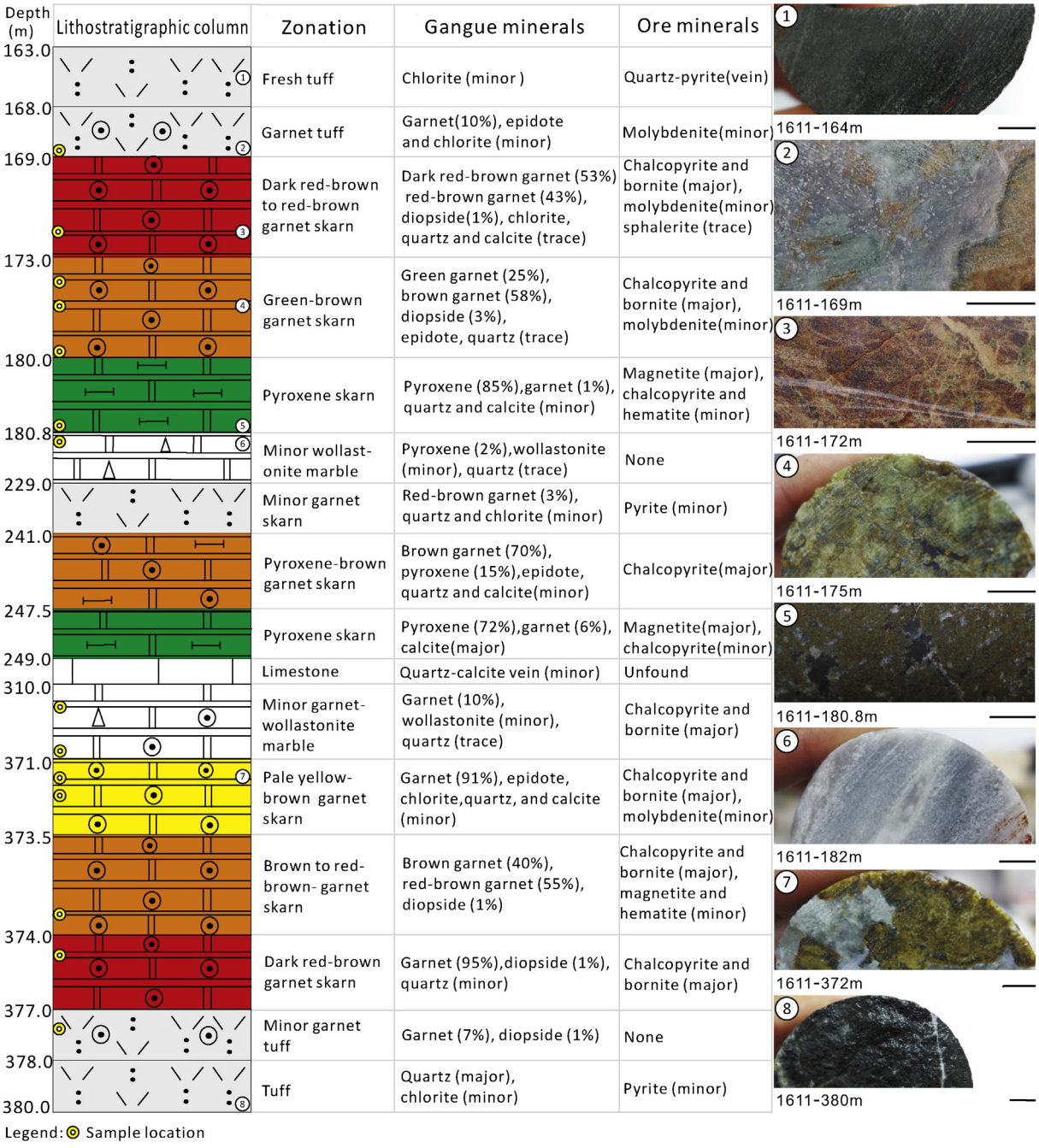

Fig. 5. Lithostratigraphic column and zonation of skarn in drill hole ZK1611. The description and scale bars are the same as in Fig. 4.

disseminated in interstitial early minerals (Fig. 6b-c) or in quartz–chalcopyrite–pyrite veins and quartz–chalcopyrite–bornite veins (Fig. 6d). The mineral paragenesis for the Zhibula deposit is shown in Fig. 7.

4. Samples and analytical methods

4.1. Electron probe microanalyses

Some representative samples of endoskarn and exoskarn were taken from the drill holes ZK2014 and ZK1611 (drill hole locations are shown in Fig. 2b; the locations of the drill hole samples are shown in Figs. 4 and 5) and were prepared as polished thin sections for subsequent examination with optical microscopy. Then, representative polished thin sections were carbon-coated for electron probe microanalysis (EPMA). Combined with previous work (ref., Xu et al., 2014), samples of 18 garnet skarns and 7 pyroxene skarns and points of 38 garnets and 12 pyroxenes were analyzed with EPMA. The compositions of the garnet and pyroxene were determined at the Electron Probe Laboratory of the China University of Geosciences, Beijing (CUGB) by using an EPMA-1600 electron probe with a 15 kV accelerating voltage, 1×10^{-8} Å beam current, and 1 μm beam spot. The natural mineral or synthetic metal was adopted as the standard with accuracy better than 0.01%. The chemical formulae of the garnet and pyroxene were obtained by using the method of oxygen atom calculation (Deer et al., 1992) and the ratios of Fe^{2+} and Fe^{3+} were obtained based on the balance of electrovalence (Droop, 1987). The results are listed in Table 1.

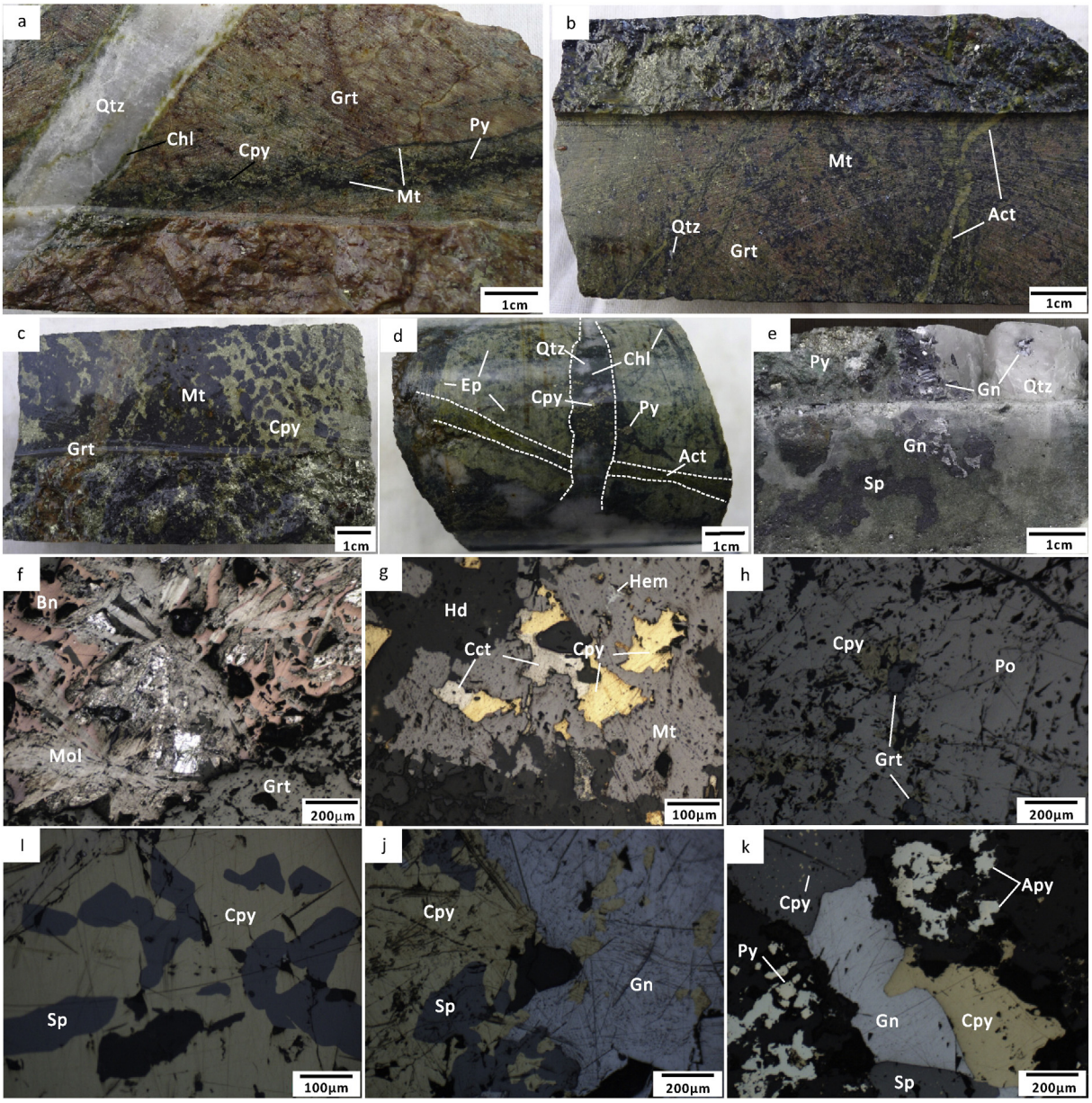

Fig. 6. Typical ores and minerals in the Zhibula deposit. a. Dark red-brown garnet skarn was cross-cut by a fine magnetite vein. Both were cross-cut by a later fine chalcopyrite–pyrite vein, followed by the latest chlorite–quartz vein. b. Dark red-brown garnet crystals were replaced by disseminated magnetite and actinolite along the intergranular fissuring and were filled by actinolite micro-vein. c. Replacement of dark red-brown garnet by magnetite, with residual garnet in veins. Stage III chalcopyrite was filled interstitially in garnet and magnetite. d. An actinolite vein cut epidote skarn, and both were cross-cut by a later quartz–chlorite–chalcopyrite–pyrite vein. e. Galena, sphalerite, and quartz of stage III in the skarn. f. Radial pattern that indicates that euhedral molybdenite and anhedral red bornite were filled interstitially in garnet crystals. g. Replacement of magnetite by sharp hematite in interstitial hedenbergite. Chalcocite follows a smooth contact with chalcopyrite. h. Chalcopyrite replaced the pyrrhotite along the crystal boundaries, which indicates that the chalcopyrite was later than the pyrrhotite. The metasomatic residual texture of the garnet is shown. i. Sphalerite substituted for chalcopyrite, suggesting that chalcopyrite formed earlier than sphalerite. j. Replacement of chalcopyrite by later galena and sphalerite. k. Euhedral pyrite and arsenopyrite crystals. Galena replaced the chalcopyrite. Chalcopyrite blebs were in sphalerite, comprising the solid-solution series. Mineral symbols: Hd, Hedenbergite; Act, Actinolite; Chl, Chlorite; Hem, Hematite; Po, Pyrrhotite; Mol, Molybdenite; Py, Pyrite; Apy, Arsenopyrite; Cpy, Chalcopyrite; Cct, Chalcocite; Bn, Bornite; Sp, Sphalerite; Gn, Galena. a–e are hand specimen photographs and f–k are microphotographs under reflected light.

4.2. Fluid inclusion analyses

Based on clear metallogenic stages, representative samples from different stages are used for fluid inclusion studies (a detailed description is shown in Fig. 9). Detailed investigations of fluid inclusions in garnet, pyroxene, epidote, quartz, and calcite were conducted on more than 30 doubly polished thin sections. The microthermometric analyses of epidote, quartz, and calcite were performed by using a Linkam THMS 600 heating–freezing stage, which has a measured temperature range from −180 °C to +600 °C, at the State Key Laboratory of Geological Process and Mineral Resources (GPMR), CUG, Wuhan. The heating rates were 0.1 °C/min when the phase transitions were approached. The errors were ±0.2 °C and ±5 °C for the final ice melting and homogenization temperatures, respectively. The microthermometric analyses of garnet and pyroxene were performed by using Linkam TS1500 (~1500 °C) in the Fluid Inclusion Laboratory of CUG, Beijing. The microthermometric measurements of the fluid inclusions followed the procedure of Shepherd et al. (1985).

The vapor and liquid compositions of individual fluid inclusions were analyzed by using the Renishaw MK1-1000 laser Raman microspectrometer at GPMR, CUG, Wuhan. An Ar^{+} laser with a wave length of 532 nm was used as the laser source with a power of 22 mW. The spectrum diagram was taken from the wave band of 100–4000 cm^{-1}. The spectral resolution was ±2 cm^{-1} with a

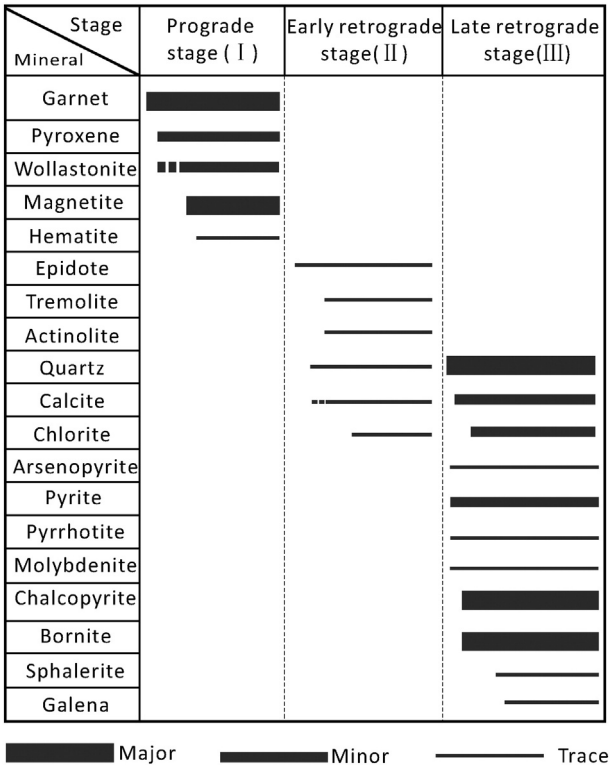

Fig. 7. Mineral paragenesis for the Zhibula Cu skarn deposit.

beam size of 1 μm. The instrumental settings were kept constant during the analysis.

4.3. Stable isotope analyses

Mineral separates of chalcopyrite, bornite, molybdenite, sphalerite, galena, and pyrite, each 0.25–0.42 mm in size, were prepared with careful handpicking under a binocular microscope with a purity of 99%, followed by cleaning in doubly distilled water. The bulk rocks of tuff, marble, monzogranite, and granodiorite were crushed into 200 mesh. The sulfur isotopic compositions were analyzed at the Analytical Laboratory of Beijing Research Institute of Uranium Geology on a Finnigan MAT-251 isotope mass spectrometer. The sulfide samples were directly oxidized to SO_2 to feed into the instrument with Cu_2O (Robinson and Kusabe, 1975). The results are expressed relative to the international standard V-CDT with a precision better than ±0.2‰.

Separates of garnet, magnetite, quartz, and calcite grains from different stages were prepared with careful handpicking under a binocular microscope to achieve a purity of 99%. Then, each of these separates was crushed into 40–60 mesh and 200 mesh for hydrogen and oxygen isotope analyses, respectively. Both the hydrogen and oxygen isotope analyses were performed by using a MAT-253 EM spectrometer at the Isotopic Laboratory of the Institute of Mineral Resources, Chinese Academy of Geological Sciences, Beijing, China. The hydrogen isotope analysis involved the release of water from fluid inclusions by crushing; this water was then reacted with zinc for 30 min at a temperature of 400 °C to produce hydrogen (Coleman et al., 1982), which was transferred to a sample bottle that was filled with activated carbon after freezing in liquid nitrogen. Oxygen isotopes were measured by using the conventional BrF_5 method (Clayton and Mayeda, 1963), and the resultant oxygen reacted with graphite rods to produce carbon dioxide. All the resulting values are reported relative to the V-SMOW standard, with an error of ±0.2‰ for $\delta^{18}O$ and of ±2‰ for δD.

Table 1
Representative electron microprobe analyses of garnet, pyroxene from the Zhibula Cu skarn deposit.

Sample	1611-179-1	1611-179-2	1611-179-3	1611-179-4	2014-1	2014-2	2014-3		2014-4	2014-5	2014-6	2014-7
	Green garnet				Garnet in the intrusion				Pyroxene in the intrusion			
SiO_2	36.69	37.66	37.21	37.94	37.60	36.90	37.32	SiO_2	51.54	52.42	53.31	53.41
TiO_2	0.02	0.00	0.15	0.10	0.00	0.48	0.54	TiO_2	0.16	0.00	0.40	0.00
Al_2O_3	0.71	3.58	1.30	5.76	5.18	2.62	3.37	Al_2O_3	1.06	0.39	0.16	0.27
FeOT	29.28	25.88	27.84	23.52	24.84	27.79	27.76	FeOT	9.12	8.89	8.34	9.12
MnO	0.19	0.32	0.18	0.05	0.70	0.57	0.48	MnO	0.88	0.52	0.42	0.19
MgO	0.24	0.16	0.16	0.12	0.00	0.00	0.12	MgO	13.17	13.37	13.89	14.19
CaO	32.76	33.01	32.81	33.45	31.38	30.78	30.69	CaO	22.94	22.83	23.30	22.68
Na_2O	0.15	0.00	0.13	0.05	0.00	0.09	0.02	Na_2O	0.38	0.55	0.63	0.68
K_2O	0.03	0.00	0.01	0.00	0.00	0.00	0.03	K_2O	0.00	0.07	0.00	0.02
Total	100.12	100.54	99.93	100.85	99.48	99.03	100.4	Total	99.25	99.04	100.5	100.6
	Cations on the basis of 12 oxygen atoms								Cations on the basis of 6 oxygen atoms			
Si	3.27	3.25	3.29	3.21	3.24	3.26	3.24	Si	1.96	1.99	1.99	1.99
Ti	0.00	0.00	0.01	0.01	0.00	0.03	0.04	Ti	0.00	0.00	0.01	0.00
Al	0.07	0.36	0.14	0.57	0.53	0.27	0.35	$Al^{(iv)}$	0.04	0.01	0.01	0.00
Fe^{3+}	1.96	1.59	1.79	1.42	1.41	1.63	1.55	Fe^{3+}	0.09	0.08	0.07	0.09
Fe^{2+}	0.05	0.15	0.11	0.15	0.27	0.28	0.34	Fe^{2+}	0.20	0.20	0.19	0.19
Mn	0.01	0.02	0.01	0.00	0.05	0.04	0.03	Mn	0.03	0.02	0.01	0.01
Mg	0.02	0.01	0.01	0.01	0.00	0.00	0.01	Mg	0.74	0.76	0.77	0.79
Ca	2.87	2.85	2.87	2.85	2.73	2.71	2.67	Ca	0.93	0.93	0.93	0.90
Na	0.02	0.00	0.02	0.01	0.00	0.01	0.00	Na	0.03	0.04	0.05	0.05
K	0.00	0.00	0.00	0.00	0.00	0.00	0.00	K	0.00	0.00	0.00	0.00
Pyr	0.85	0.54	0.60	0.38	0.00	0.00	0.43	Di	80.06	77.71	79.04	80.14
Spe	0.65	1.03	0.64	0.15	2.23	1.98	1.63	Hd	23.19	24.29	23.10	21.89
Alm	2.31	1.63	0.00	3.77	4.01	3.27	4.11	Jo	12.57	7.08	5.89	2.79
Pra	3.81	3.20	1.24	4.30	6.24	5.25	6.16					
Gro	0.00	21.73	6.16	32.29	28.35	13.51	17.36					
And	96.19	75.07	92.60	63.41	65.41	81.24	76.47					

Notes: Ura, Uvarovite; Pyr, Pyrope; Spe, Spessartine; Alm, Almandine; Pra, sum of Alm, Pyr and Spe; Gro, Grossular; And, Andradite; Di, Diopside; Hd, Hedenbergite; Jo, johannsenite; FeOT, total iron; 0.00, below the detection limit. Analysis precision is 0.0 n.

5. Analytical results

5.1. Skarn mineralogy

5.1.1. Garnet

The garnet crystals are dodecahedral and trisoctahedral, euhedral to subhedral, and medium- to coarse-grained (up to 5 mm). The garnet exhibits various colors, such as dark red-brown, red-brown, green, brown, and pale yellow-brown (Figs. 8a-c, 9a-c). The crystals exhibit optical anisotropy, chaotic birefringence, and oscillatory zoning under crossed polarized light. Most ore minerals, particularly magnetite, occur in dark red-brown and red-brown garnet skarn. Magnetite in the garnet-dominated skarn and in the ore replaced garnet along the crystal boundaries, causing the pseudomorphism of the garnet grains, or cross-cut and filled the garnet through fractures and fissures (Fig. 6b-c). The replacement and fracture filling of garnet and magnetite by minor ore minerals such as chalcopyrite, bornite, and molybdenite can be observed in green and brown garnet skarn (Figs. 6a,c, 8a-c). Only bornite can be observed in the interstitial yellow-brown garnet. Detailed examination of drill cores show that the garnet near the gray

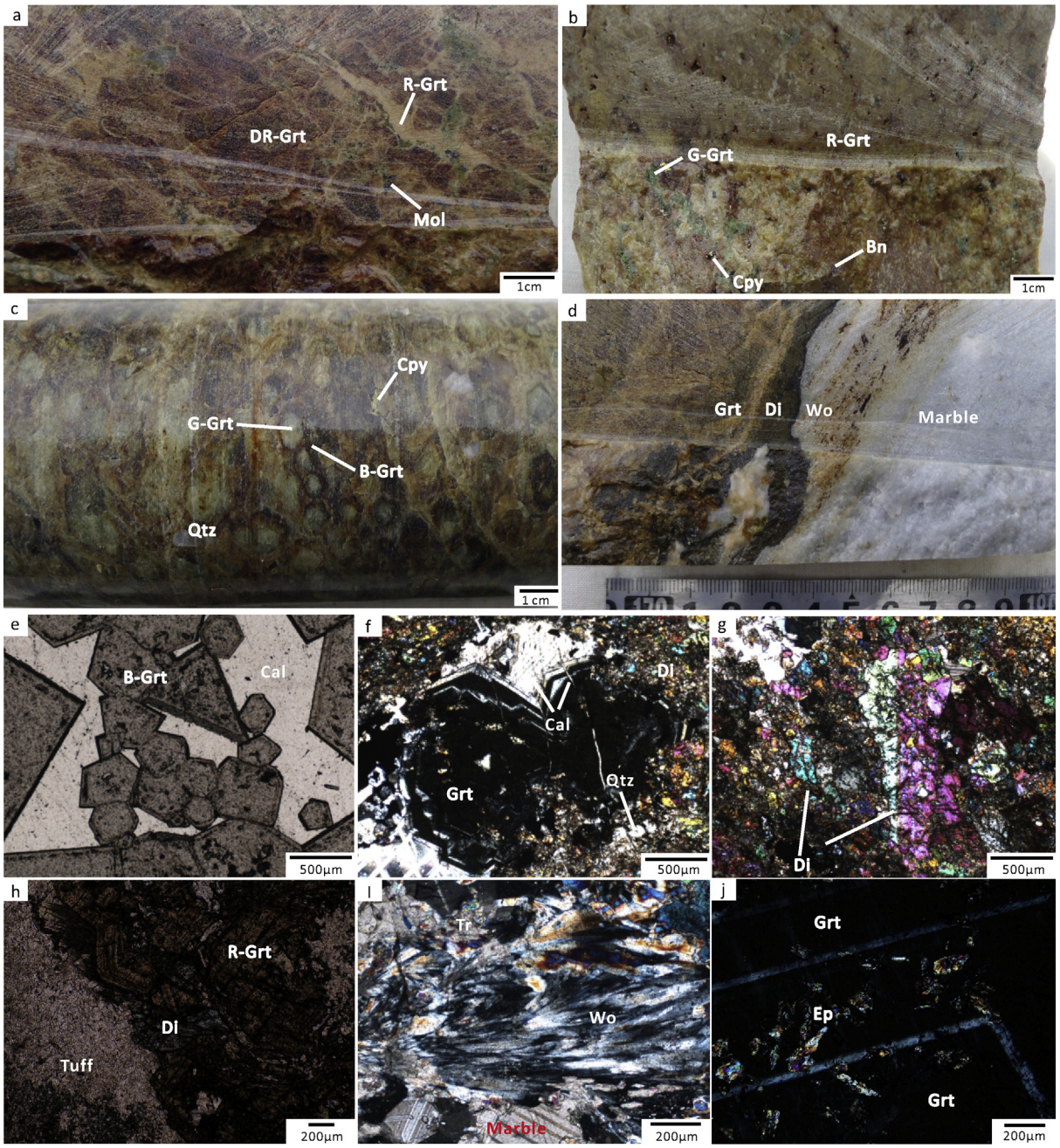

Fig. 8. Representative hand specimen photographs and photomicrographs for drill core samples. a. The dark red-brown garnet formed earlier than red-brown irregular garnet vein. Molybdenite occurred in interstitial garnet. b. Minor green garnet crystals were filled interstitially in red-brown garnet, which indicates that red-brown garnet formed earlier than green garnet. The garnet skarn contains minor chalcopyrite and bornite. c. The core of the garnet crystal is green and the rim is brown garnet, which suggests brown garnet formed later than green garnet. This feature was caused by the overgrowth of the garnet crystal rather than the alteration of the garnet crystal core. d. Local spatial relationship of garnet, pyroxene, and marble. e. Calcite was filled interstitially in euhedral garnet crystals. f. Replacement of euhedral garnet crystals by pyroxene, quartz, and calcite. Micro-vein calcite cross-cuts the garnet. g. Tabular and granular pyroxene crystals show simple twins and clustered twins. h. Subhedral red-brown garnet and diopside occur in tuff. i. Tremolite and wollastonite occur in marble. j. The garnet was replaced by fine-grained epidote. Mineral symbols: DR-Grt, Dark red-brown garnet; R-Grt, Red-brown garnet; G-Grt, Green garnet; B-Grt, Brown garnet; Tr, Tremolite; Wo, Wollastonite; Cal, Calcite. a–d are hand specimen photographs, e and h are microphotographs under plane polarized light, and f, g, i, and j are microphotographs under crossed polarized light.

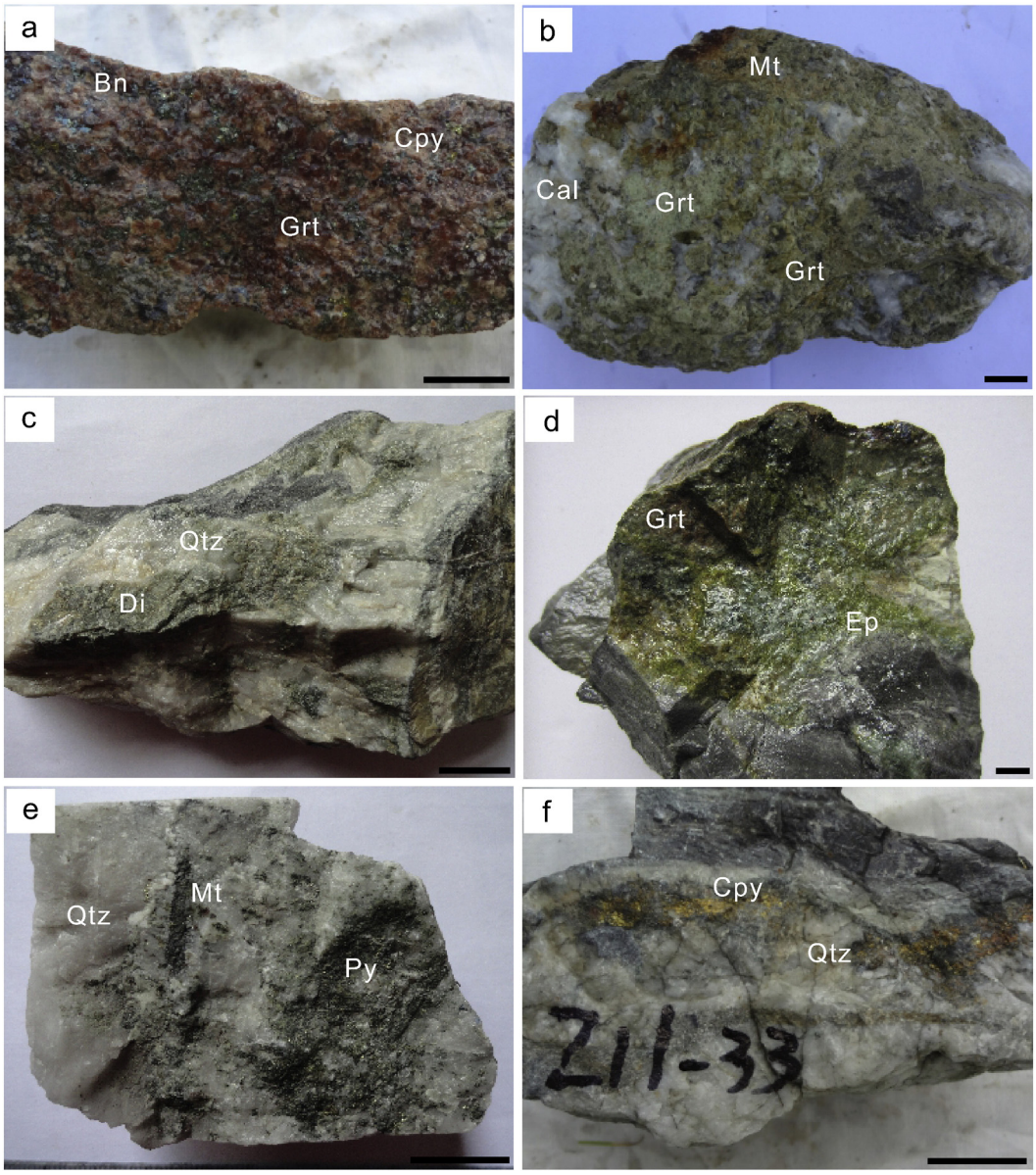

Fig. 9. Representative hand specimen photographs for the study of fluid inclusions. a. Dark red-brown garnet skarn (stage I). b. Green garnet (stage I) was altered to minor magnetite and calcite (stage II). Bulky euhedral calcite (stage III) was superimposed onto garnet. c. Pyroxene (stage I) was replaced by quartz (stage III). d. Epidote (stage II) occurred in the contact between dark red-brown garnet skarn and tuff. e. Magnetite was enclaved (stage II) in a quartz–pyrite vein (stage III). f. Quartz–chalcopyrite vein (stage III). The scale bars in all the photographs are one centimeter in length.

to black tuff is primarily dark red-brown and red-brown, whereas the garnet that is adjacent to off-white marble is more green and pale yellow-brown. The garnet is color zoned relative to its proximity to the fluid source or principal fluid pathways, similar to other Cu skarn deposits worldwide (e.g., Carr Fork Cu district, Atkinson and Einaudi, 1978; Coroccohuayco Cu skarn deposit, Maher, 2010), which show proximal garnet being dark red-brown and becoming more green and yellow with distance (Fig. 4-5). In general, these garnets are replaced by epidote and quartz from crystal cores to crystal rims during the retrograde stage.

Representative EPMA data for the garnets, partly from Xiao et al. (2011) and Xu et al. (2014) are shown in Table 1 and Fig. 10a-1. The samples of Xiao et al. (2011) were collected from exoskarn without other information. These samples can only represent the essential features of garnets, as shown in Fig. 10a-1. However, we collected garnets with various colors, in different mineral assemblages, and in exoskarn and endoskarn. These garnets, which are composed of andradite$_{(15–100)}$ − grossularite$_{(0–79)}$, are grandite, vary slightly in composition as follows: $Ca_{(2.67–3.28)}$ $Mg_{(0–0.11)}$ $Mn_{(0–0.09)}$ $Fe^{2+}{}_{(0–0.34)}$ $Fe^{3+}{}_{(0.28–2.07)}$ $Al_{(0–0.61)}$ $Cr_{(0–0.15)}$ $Ti_{(0–0.12)}$ $Si_{(2.93–3.29)}$ O_{12}. Garnets in various colors exhibit different end-members, beginning with dark red-brown and red-brown, then green and brown, and finally pale yellow-brown. The values of andradite increase, while the grossularite end-members decrease (Fig. 10a-2). The garnets in the endoskarn are mainly andradite, those close to the tuff are mostly composed of andradite and grossularite in a broad compositional range, and those in the front of marble generally consist of andradite in a narrow compositional range (Fig. 10a-3). Chang and Meinert (2004) proposed that magmatic hydrothermal fluids have low Al solubility, except if the fluid is F-rich. In addition, the migration ability of Al and Ti is weak because of their low mobility (Wilkinson et al., 2011). Therefore, the garnet near the tuff and intrusions will prioritize gathering Al and Ti. The Fe and Mn contents in the pale yellow-brown garnet close to the marble are higher than others, which is consistent with the composition of pyroxene (Fig. 10b). These garnets were probably affected by Fe and, particularly, Mn activity, which prefers to migrate to the distal end at low temperature.

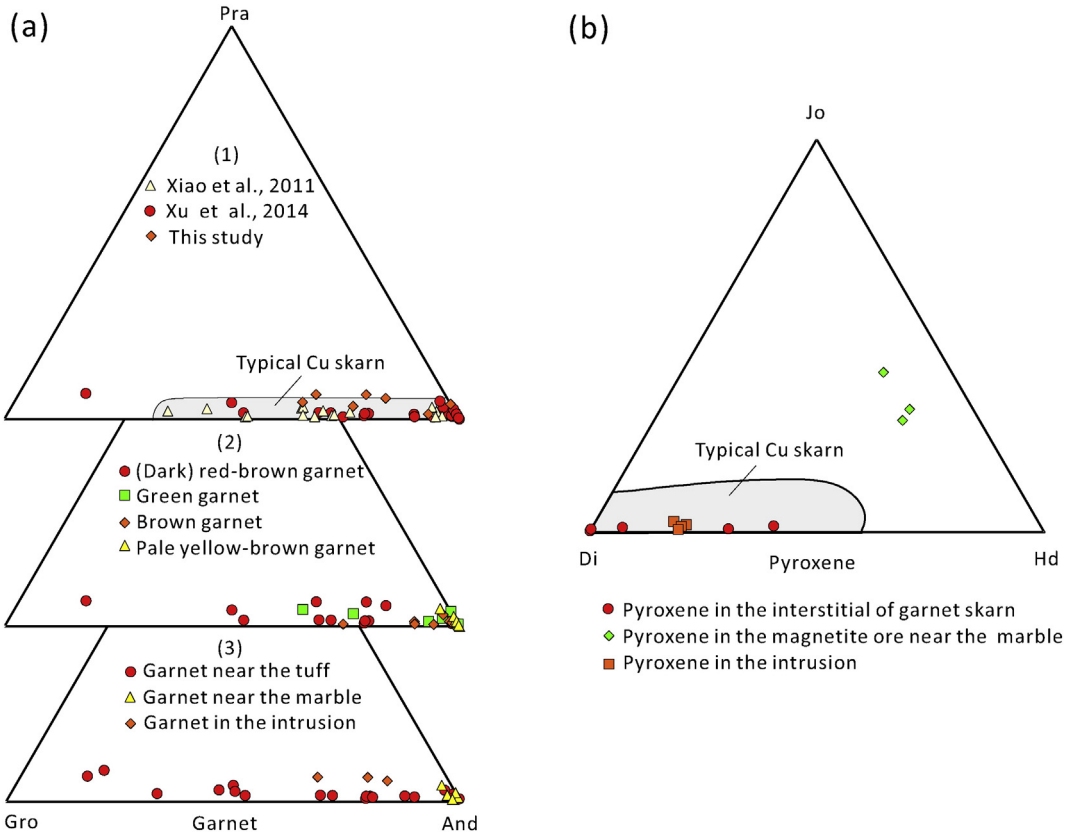

Fig. 10. End-members of garnet (a) and pyroxene (b). The data of the Zhibula garnet are partly from Xu et al. (2014) and Xiao et al. (2011). The data for typical Cu skarn are from Meinert et al. (2005).

5.1.2. Pyroxene

Pyroxene skarn is less common than garnet skarn. Dark green pyroxene crystals occur in massive aggregates or veins and are euhedral to subhedral and fine- to medium-grained (up to 2 mm) (Fig. 8f-g). Although pyroxene appears to have intergrown with garnet in most skarn, it has partially replaced the garnet (Fig. 8h,f). The pyroxene was altered to amphibole (tremolite–actinolite), magnetite, quartz, and calcite as interstitial or micro-veinlets (Figs. 8f, 9d). Pyroxene skarn generally occurs near marble and wollastonite marble (Fig. 8d).

Pyroxenes from skarn, intrusion, and marble were analyzed. Representative EPMA data, some of which were from Xu et al. (2014), are provided in Table 1 and are plotted in Fig. 10b. In general, the pyroxenes are predominantly diopside-hedenbergite (Di_{13-90} Hd_{0-51} Jo_{0-37}) and vary slightly in composition as follows: $Na_{(0.01-0.05)}$ $Ca_{(0.90-1.02)}$ $Mg_{(0.14-1.03)}$ $Fe^{2+}{}_{(0-0.50)}$ $Fe^{3+}{}_{(0.07-0.14)}$ $Cr_{(0-0.01)}$ $Al_{(0-0.04)}$ $Ti_{(0-0.01)}$ $Si_{(1.93-1.99)}$ O_6. The end-member contents of hedenbergite and johannsenite and the Mn/Fe ratios in the pyroxene crystals, which are close proximity to the marble and are rich in magnetite, are Hd_{41-51} Jo_{26-37} and 0.35–0.61, respectively, higher than those that are associated with garnet, which exhibit Hd_{0-36} $Jo_{0.7-1.4}$ and 0.02–0.06, respectively (data from previous work, Xu et al. (2014)). These results are consistent with the conclusion by Harris and Einaudi (1982) that the Mn contents in the pyroxene gradually increased close to the marble. This relationship occurred because the mobility of Mn is affected by the temperature and because Mn prefers to migrate and gather in low temperature fluids at distal places. However, this observation cannot exclude the influence from the composition of the marble.

5.2. Fluid inclusions

5.2.1. Petrography

A proper interpretation of fluid inclusions (FI) can be made only when the textural relationships between FIs and the host mineral are considered. Without the right context, even huge numbers of microthermometry and analytical data do not contribute much to reveal the rock-forming conditions (Van den Kerkhof and Hein, 2001). Three FI types were identified based on the phase within the FIs at room temperature (average 25 °C) and the phase transformation characteristics during the freezing and heating process, including (1) type L (approximately 55–65% content), which is represented by two-phase, liquid-rich FIs with <50 vol.% of bubbles (vapor–liquid, V-L) and homogenization to a liquid phase; (2) type V (approximately 10–20% content), which is represented by two-phase, vapor-rich FIs with >50 vol.% of bubbles (liquid–vapor, L-V) and homogenization to a vapor phase; and (3) type S (approximately 15–25% contents), which is represented by three-phase FIs (solid–liquid-vapor, S-L-V). According to the types of daughter minerals and their homogenization nature, the type S FIs can generally be divided into four types: the halite daughter of type S_1 dissolves before vapor disappearance; the halite dissolution of type S_2 occurs later than vapor disappearance upon heating; type S_3 contains both halite and sylvite daughters and the halite dissolution is later than vapor disappearance; and type S_4 contains opaque minerals, such as magnetite or hematite. Representative minerals in different stages were collected for FI study (the samples and descriptions are shown in Fig. 11). The characteristics of each stage are described as follows (Table 2).

Stage I: FIs in garnet and diopside are used to study the early fluids. The FIs in the garnet are only rarely preserved, as noted in several other skarn deposits (e.g., Big Gossan Cu–Au deposit, Meinert et al., 1997; Nambija Au deposit, Vallance et al., 2009; Baiyinnuo'er Zn–Pb deposit, Shu et al., 2013) and can be divided into type L (Fig. 11a) and type S_4 (Fig. 11b). The primary FIs are small (7–15 μm) hexagons or irregular squares with 5–30 vol.% of bubbles. Most of them are secondary FIs (13–45 μm), and few red hematites can be observed (Fig. 11b). Types L, S_1, and S_4 are recognized in diopside (Fig. 11c,d). The primary FIs are squares, ellipsoids, or irregular in shape with sizes that range from

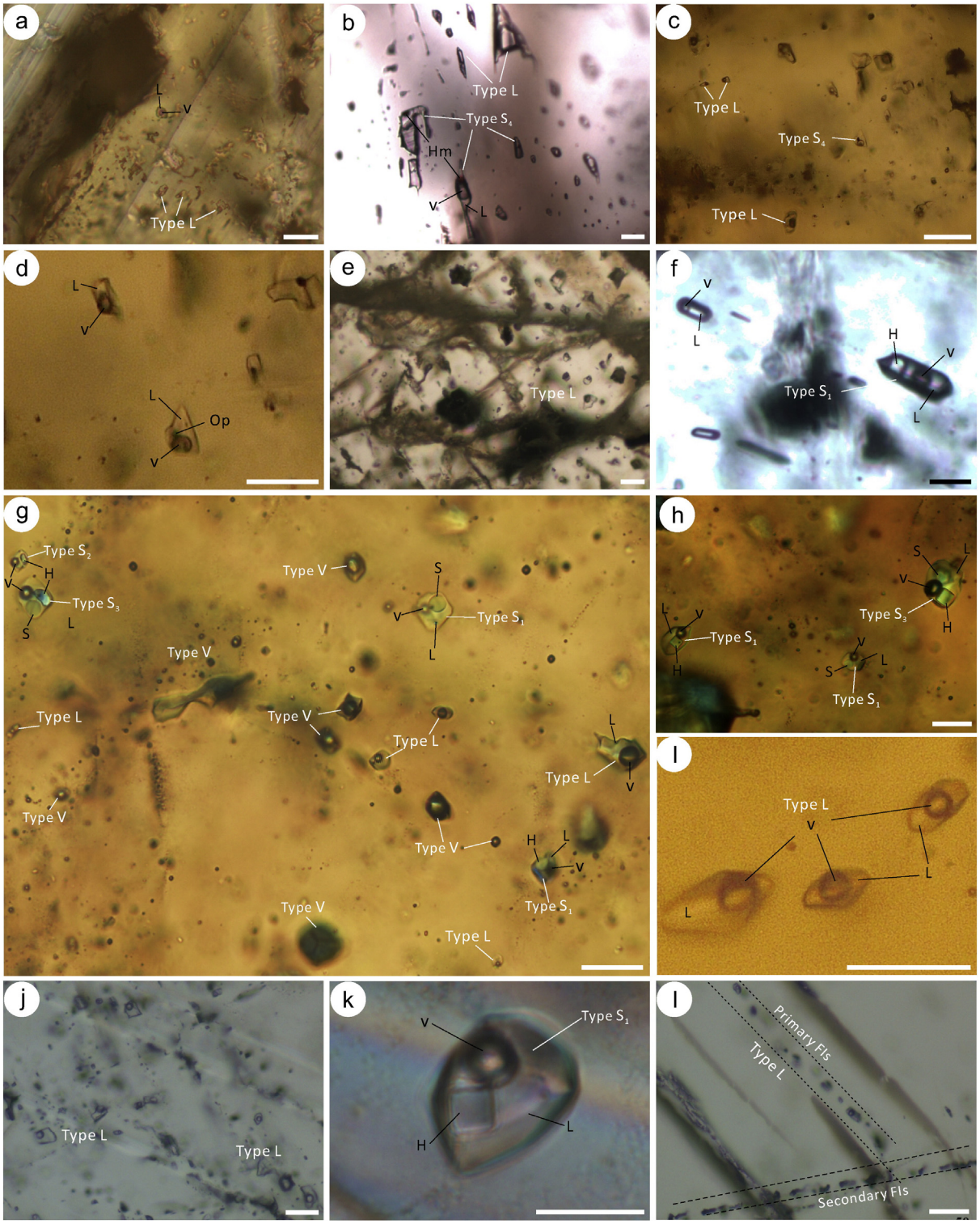

Fig. 11. Photomicrographs of different types of representative fluid inclusions in different stages. a. Minor primary type L in garnet zoning (stage I). b. Abundant secondary type L and type S_4 (hematite-bearing) coexist in garnet (stage I). c. Coexistence of primary type L and type S_4 (opaque mineral-bearing) in pyroxene (stage I). d. Type L and type S_4 in pyroxene. e. Abundant primary type L in epidote (stage II). f. Coexistence of type L and type S_1 (halite-bearing) in epidote. g. Type L, type V, type S_1 (sylvite-bearing), type S_2 (halite-bearing), and type S_3 coexist in quartz (stage III). h. Coexistence of type S_1 (halite-bearing) and type S_3 (halite–sylvite-bearing) in quartz. i. Negative crystal type L in quartz. j. Abundant type L in calcite (stage III). k. Type S_1 (halite-bearing) in calcite. l. Primary and secondary FIs in calcite (stage III). Mineral symbols: L, liquid phase; V, vapor phase; Op, opaque mineral; H, halite; S, sylvite. The scale bars in all the photographs are 20 μm in length.

10 to 44 μm. The bubble volume of type L is 8–35 vol.% and that of the type S inclusions is approximately 30–35 vol.%. The daughter minerals in type S can be divided into transparent and opaque. The transparent daughter minerals are cubic halite crystals (type S_1), whereas the opaque ones are inferred to be magnetite (type S_4).

Stage II: Epidote was chosen to constrain the fluid signatures of the early retrograde stage. Although type V (approximately 30% content) and type S_1 (approximately 10% content) developed in epidote (Fig. 11e-f), type L (approximately 60% content) is predominant. Type L can also be observed coexisting with type V and type S_1 in epidote

Table 2
Microthermometric data of fluid inclusions in different stages from the Zhibula Cu skarn deposit.

Stage	Host mineral	P and S	Type	Size/μm	V/vol%	Tm(ice)/°C (N)	Tm(s)/°C	Tm(h)/°C	Td(bub)/°C	Th/°C (N)	H-style	Salinity
I	Grt	P	L	10	5					613 (1)	Liquid	
		S	L	13–45	5–30	−2.7 to −5.0 (3)				137–394 (19)	Liquid	4.5–7.9
	Di	P	L	10–44	8–35	−3.9 to −12.3 (24)				405–667 (40)	Liquid	6.3–16.2
		P	S_1	44	30			376	576	576 (1)		44.0
II	Ep	P	L	15–50	8–30	−3.5 to −11.2 (12)				402–595 (12)	Liquid	5.7–15.1
		P	V	16–40	50–55	−6.8 to −13.7(8)				443–523 (8)	Vapor	10.2–17.5
		P	S_1	38–50	30			314–438	488–509	488–509(2)		39.0–50.0
III	Q	P, PS	L	15–50	7–44	−2.4 to −14.5 (55)				250–420 (93)	Liquid	4.0–18.2
		P	V	10–55	50–70	−7.3 to −14.6 (4)				303–384 (13)	Vapor	10.9–18.3
		P	S_1	20–40	15–45			163–300	266–350	266–350 (10)		30.2–37.9
		P	S_2	15–55	15–30			250–380	108–310	250–380 (16)		34.6–44.2
		P	S_3	30–40	25		131–256	282–325	205–229	282–325 (3)		36.6–39.7
	Cc	P, PS	L	13–50	8–35	−0.5 to −8.9 (32)				194–318 (52)	Liquid	0.9–12.7
		P	V	36–46	40	−6.7 to −7.9 (3)				250–288 (4)	Vapor	10.1–11.6
		P	S_1	24–28	15			156–163	204–206	204–206 (2)		30.0–30.3

Notes: N, Number of inclusions analyzed; Tm (ice), Final ice melting temperature; Tm (h), Halite melting temperature; Tm (s), Sylvite melting temperature; Td (bub), Bubble disappear temperature; Th, Total homogenization temperature; H-style, Style of homogenization; P, Primary; S, Secondary; Ps, Peuclosecondary; Salinity expressed as wt.% NaCl equiv.

(Fig. 11f). The primary inclusions are negative crystals (Fig. 11f) that, range from 15 to 50 μm. Generally, these inclusions are distributed in assemblages. The bubble volumes of type L, V, and S_1 are 8–30 vol.%, 50–55 vol.%, and 30–35 vol.%, respectively. The daughter minerals in type S_1 are cubic halite.

Stage III: Because the quartz and calcite show a paragenetic relationship with sulfides such as chalcopyrite, bornite, galena, and sphalerite (Figs. 6d-e and 9f), the FIs in quartz and calcite are the best choices. The primary FIs are negative crystals, tubes, squares, ellipsoids, or irregular in shape, vary from 10 to 55 μm and occur as isolated inclusions or groups. All types of FIs can be observed in quartz and calcite (Fig. 11g-k), including type L (approximately 45% content), type V (approximately 25% content), and type S (approximately 30% content). Type L coexists with type V and type S in one field of vision under the microscope

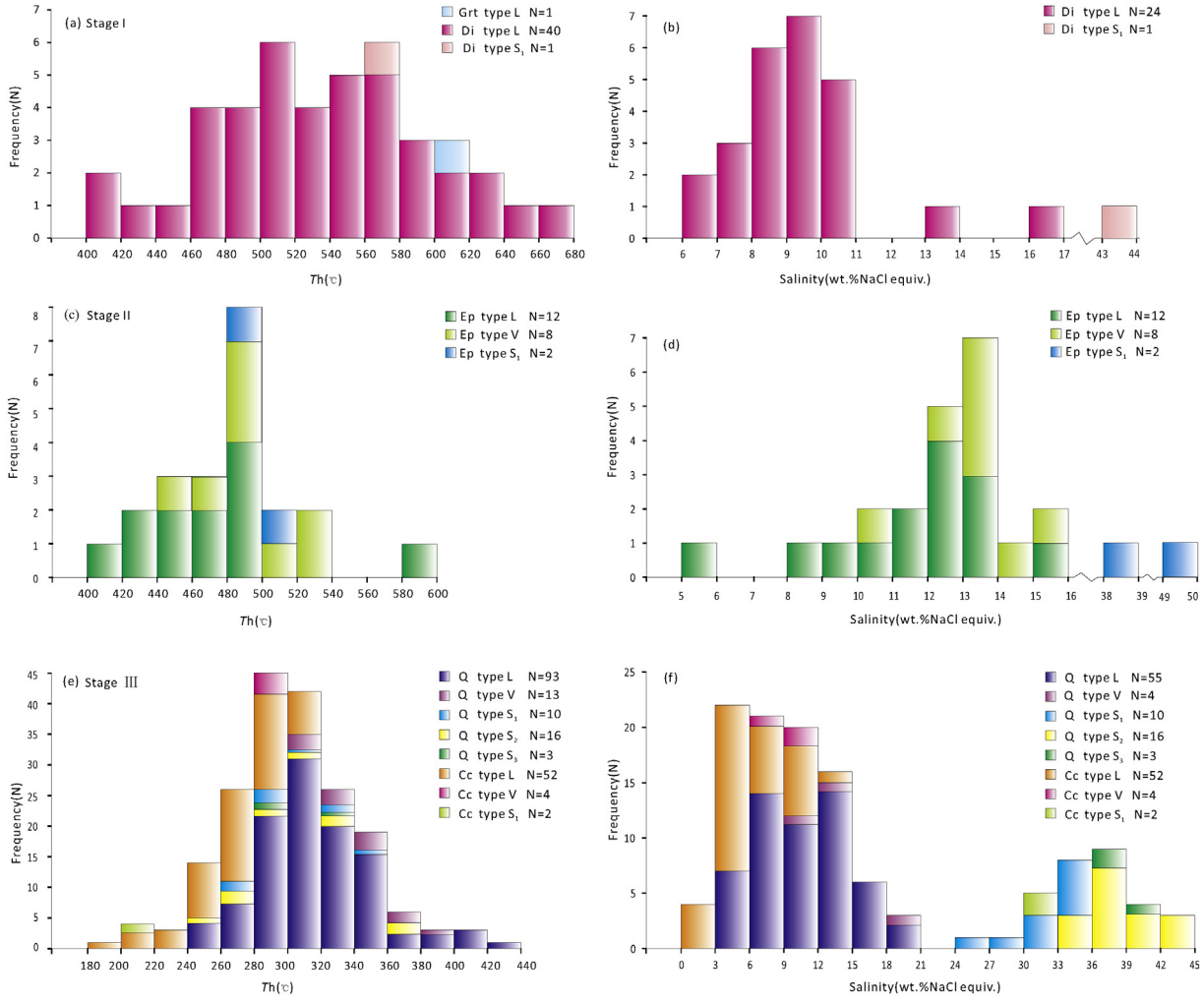

Fig. 12. Homogenization temperature and salinity histograms of all the inclusion types separated into different stages and host minerals.

(Fig. 11g). Bubbles generally comprise 7–44 vol.% of the type L, 50–70 vol.% of the type V, and 15–45 vol.% of type S inclusions. The daughter minerals in type S are cubic halite and rounded sylvite.

5.2.2. Microthermometry

Although sylvite daughter minerals were observed in the quartz FIs (S_3-type), they were relatively rarer than other types of FIs. In addition, no CO_2–H_2O FIs developed in any stages; thus, the ore-forming fluids broadly correspond to a NaCl–H_2O system. The salinities of type L and V were calculated by using the NaCl–H_2O system equation that was provided by Bodnar (1993). For halite-bearing inclusions (type S_1, S_2, and S_3), the equation of Sterner et al. (1988) was used to estimate their salinities when assuming a NaCl–H_2O system. The salinities of all the FIs were reported as wt.% NaCl equiv. Detailed microthermometry data are listed in Table 2 and shown in Fig. 12.

Stage I (Fig. 12a-b): Most of type L inclusions in the garnet are secondary FIs with homogenization temperatures that vary from 137 to 394 °C and ice-melting temperatures that range from −2.7 to −5.0 °C, which correspond to salinities from 4.5 to 7.9 wt.% NaCl equiv. (Table 2). Because secondary FIs are not the typical fluid feature of this stage, we will not discuss the features of these secondary FIs. The primary FIs in the garnet and diopside show homogenization temperatures that vary 405 to 667 °C and ice-melting temperatures that range from −3.9 to −12.3 °C, which correspond to salinities from 6.3 to 16.2 wt.% NaCl equiv. Only one type S_1 was measured because of their poor preservation during this stage. This inclusion's homogenization temperature was 576 °C and its halite dissolution temperature was 376 °C, which correspond to a salinity of 44.0 wt.% NaCl equiv.

Stage II (Fig. 12c-d): The homogenization temperatures, ice-melting temperatures, and salinities are 402–595 °C, −3.5 to −11.2 °C, and 5.7–15.1 wt.% NaCl equiv. for type L; 443–523 °C, −6.8 to −13.7 °C, and 10.2–17.8 wt.% NaCl equiv. for type V; and 488–509 °C, 314–438 °C, and 39.0–50.0 wt.% NaCl equiv. for type S_1, respectively (Table 2).

Stage III (Fig. 12e-f): Type L inclusions are abundant in quartz and calcite. The homogenization temperatures of the quartz and calcite vary from 250 to 420 °C and from 194 to 318 °C, respectively (Table 2). The ice melting temperature vary from −2.4 to −14.5 °C and from −0.5 to −8.9 °C, which indicates that the salinities are 4.0–18.2 and 0.9–12.7 wt.% NaCl equiv. Type V inclusions are also abundant and have homogenization temperatures of 303–384 °C and 250–288 °C in quartz and calcite, respectively. Their ice melting temperatures range from −7.3 to −14.6 °C and from −6.7 to −7.9 °C, which correspond to low salinities of 10.9–18.3 and 10.1–11.6 wt.% NaCl equiv. The type S inclusions in the quartz and calcite exhibit homogenization temperatures that vary from 250 to 380 °C and from 204 to 206 °C, halite dissolution temperatures from 163 to 300 °C and from 156 to 163 °C, and salinities from 30.2 to 44.2 and from 30.0 to 30.3 wt.% NaCl equiv. However, the homogenization temperatures of quartz (250–420 °C) during this stage were relatively higher than those of calcite (194–318 °C).

5.2.3. Pressure estimation

Previous studies (Roedder and Bodnar, 1980; Shepherd et al., 1985; Brown and Hagemann, 1995) indicated that the trapping pressure can be estimated only when the exact trapping temperature is known or when fluid inclusions are trapped during phase separation. During stages I and II, coexisting type S_1, L, and V homogenized to similar temperatures, as described by Baker and Lang (2003) when they studied the fluids in the Bismark skarn deposit at Mexico, which indicates that immiscibility occurred. Hedenquist et al. (1992) concluded that the petrological criteria for boiling caused the vapor-rich FIs to homogenize to a vapor phase, which are closely spatially associated with the liquid-rich FIs that homogenize to a liquid phase and show similar homogenization temperatures. During stage III, the coexisting type V, S, and L in quartz and calcite and similar homogenization temperatures show the characteristics of boiling inclusion assemblages. These inclusion assemblages also imply that liquid and vapor were separated from a single-phase fluid. Therefore, their exact trapping pressures were estimated by the formula that was provided by Driesner and Heinrich (2007). The trapping pressures were mostly between 500 and 600 bar during stage I, 400–600 bar during stage II, and 250–350 bar during stage III (Fig. 13a).

The empirical equation that was proposed by Becker et al. (2008) was used for type S_2 inclusions. The minimum trapping pressures are heterogeneous and vary from 500 to 2000 bars (Fig. 13b), which are significantly higher than those of type S_1. Type S_2 has been observed in many skarn and porphyry deposits (Cline and Bodnar, 1994; Zhang et al., 2007; Klemm et al., 2008; Shu et al., 2013). This type can either be formed by direct exsolution from parent magma (Cline and Bodnar, 1994; Zhang et al., 2007), trapped after undergoing overpressuring (Baker and Lang, 2003), or achieved through a process of post-entrapment modification (Klemm et al., 2008). These FIs in the Zhibula deposit coexist with type S_1 and have analogous homogenization temperatures with low-salinity FIs, which indicates that they were generated from the post-entrapment modification of type S_1 because of H_2O loss (Audétat and Günther, 1999).

5.2.4. Laser Raman spectroscopy

Laser Raman spectroscopy is one of the fastest and non-destructive analytical methods to test the compositions of fluid inclusions (Burke, 2001). Representative FIs were selected from different stages for laser Raman spectroscopy to constrain their compositions, and parts of the spectra are shown in Fig. 14. However, not all the FIs yielded adequate results because of the sizes of the bubbles, the depth of FIs, and the high background values of hosting minerals, particularly in calcite. The experimental results (type L and type V FIs in quartz) show that the liquid phases were dominated by H_2O (Fig. 14a-b), and no volatiles were detected. The vapor phases of these FIs were mainly composed of H_2O and CO_2 with rare CH_4 (Fig. 14c-i). The relative contents between CO_2 and CH_4 were also estimated, showing that the CO_2 contents were relatively higher than CH_4 contents (Fig. 14g-i).

5.3. Stable isotopic compositions

The sulfur isotopic results and comparative data from other studies (She et al., 2005) of the Zhibula deposit are listed in Table 3. The $\delta^{34}S_{V\text{-}CDT}$ values of the sulfides range from −0.1 to −6.8‰, with an average of −3.9‰ (n = 24). The $\delta^{34}S$ values that were obtained from the pyrite, molybdenite, sphalerite, chalcopyrite, galena, and bornite range from −0.1 to −2‰ (average −1.3‰, n = 3), from −3.1 to −3.2‰ (average −3.1‰, n = 2), from −2.5 to −4.3‰ (average −3.2‰, n = 3), from −2.8 to −6.8‰ (average −4.3‰, n = 9), from −3.9 to −6.7‰ (average −4.8‰, n = 4), and from −4.1 to −6.3‰ (average −5.1‰, n = 3), respectively. The $\delta^{34}S$ histogram shows a normal distribution, with all the data distributed in a narrow range (Fig. 15a). The paragenetic relationship of the pyrite, sphalerite, chalcopyrite, and galena and the fact that $\delta^{34}S$ (Py) > $\delta^{34}S$ (Sp) > $\delta^{34}S$ (Cpy) > $\delta^{34}S$ (Gn) (samples Z11-3 and Z11-4, Table 3) indicates an overall equilibrium of sulfur isotopes among sulfides during the evolution of the mineralization (Ohmoto, 1972). Thus, the sulfur isotopes of the ore-forming fluids were estimated by the method from Pinckney and Rafter (1972). Two coprecipitated sphalerite-galena pairs were used to obtain the total sulfur isotopic value, which was approximately −0.7‰ (Fig. 15b). The $\delta^{34}S$ values of two coprecipitated sphalerite-galena pairs were also used to estimate the formation temperature of these ore minerals by using the fractionation factors of Ohmoto and Rye (1979). Two pairs of sphalerite–galena (Fig. 6e) from stage III have $\Delta^{34}S$ values of 2.4‰ and 1.4‰, which yield isotopic equilibration temperatures of 278 °C and 449 °C, respectively. These results are consistent with the total homogenization temperatures of fluid inclusions (194–420 °C) during stage III (Table 2, Fig. 12). The sulfur isotopic compositions of the granodiorite and monzogranite range from −0.1 to −0.4‰, with an average of −0.3‰.

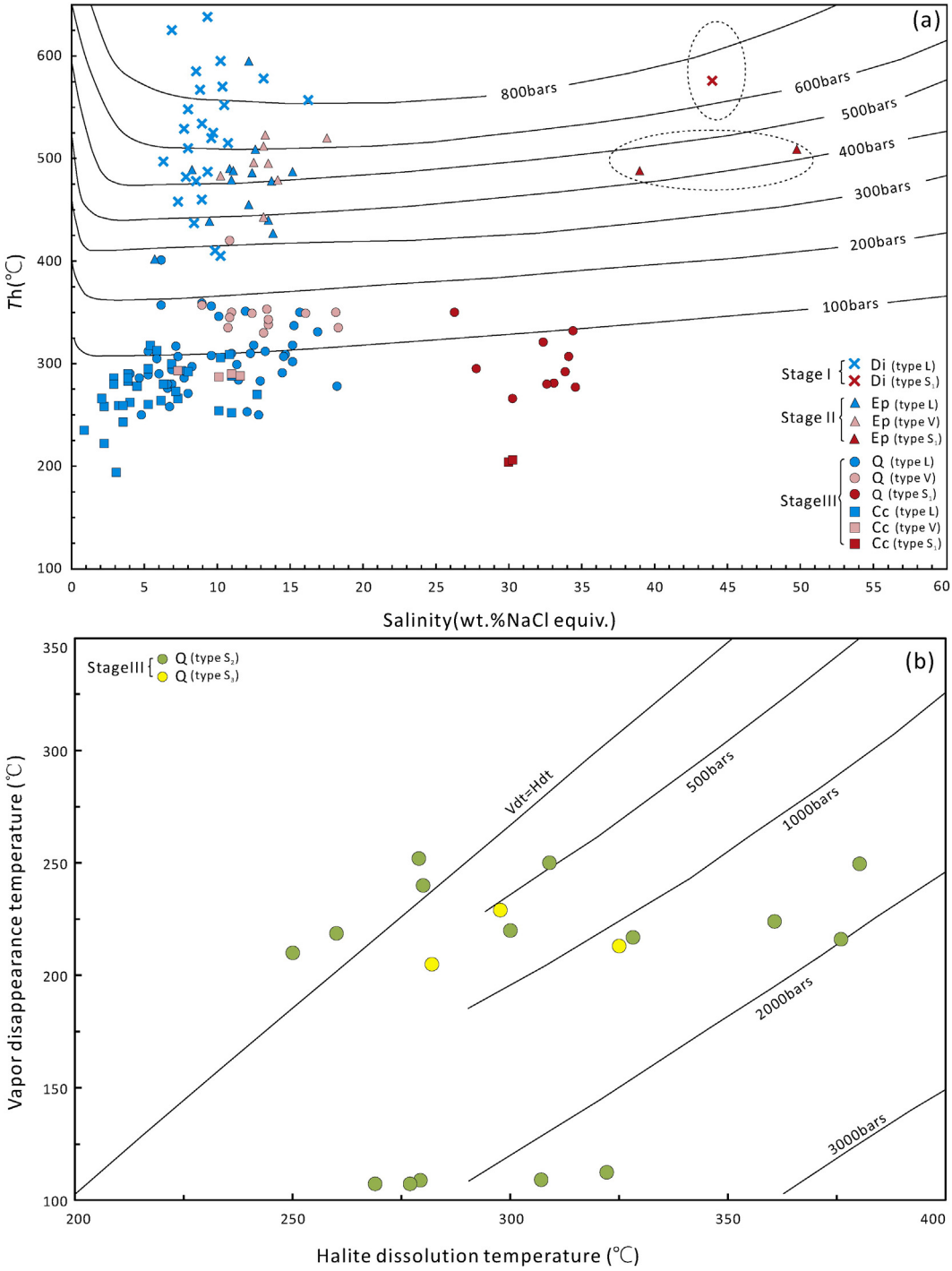

Fig. 13. Pressure estimation for fluid inclusions at stage I, stage II, and stage III. a. Type L, S_1, and V at stage I and stage II were trapped under immiscible conditions and type L, S_1, and V at stage III were trapped under boiling conditions. Thus, the estimated pressures can represent the actual trapping pressures for both. Isobars were calculated from the equations of Driesner and Heinrich (2007). b. Type S_2 and S_3 at stage III were homogenized by halite dissolution. Thus their estimated pressures only represent their minimum trapping pressures according to the phase diagram from Becker et al. (2008).

The $\delta^{34}S$ values of tuff and marble vary from −4.4 to +1.3‰ (average −2.1‰) and from +0.8 to +2.2‰ (average + 1.5‰), respectively.

The results are presented in Table 4. The δD_{H2O} and $\delta^{18}O_{Mineral}$ values, range from −91 to −159‰ and from 0.9 to 13.9‰, respectively. The calculated $\delta^{18}O_{H2O}$ values of water in equilibrium with garnet, magnetite, quartz, and calcite were based on the fractional equilibrium formulae of Taylor (1976), Zheng and Chen (2000), Clayton et al. (1972), and O'Neil et al. (1969), respectively. The calculated temperatures of the garnet, quartz, and calcite were obtained from the microthermometry of fluid inclusions, whereas the calculated temperature of magnetite was estimated by the homogenization temperature of fluid inclusions in epidote. The $\delta^{18}O_{Mineral}$ values of garnets from seven skarns in stage I were 5.2 to 5.7‰, the δD_{H2O} values were between −118 and −159‰, and the calculated $\delta^{18}O_{H2O}$ values were between 8.5 and 9.0‰. The values of $\delta^{18}O_{Mineral}$ and the $\delta^{18}O_{H2O}$ from stage II magnetite range from 0.9 to 2.2‰ and from 7.9 to 9.2‰, respectively. The $\delta^{18}O_{Mineral}$ values of six quartzes from stage III range from 7.7 to 13.9‰, the δD_{H2O} values range from −91 to −123‰, and the $\delta^{18}O_{H2O}$ values vary from 1.5 to 7.4‰. The $\delta^{18}O_{Mineral}$ value of stage III calcite was 9.0‰, the δD_{H2O} value was −113‰, and the $\delta^{18}O_{H2O}$ value was 3.0‰. In the δD vs. $\delta^{18}O_{H2O}$ diagram

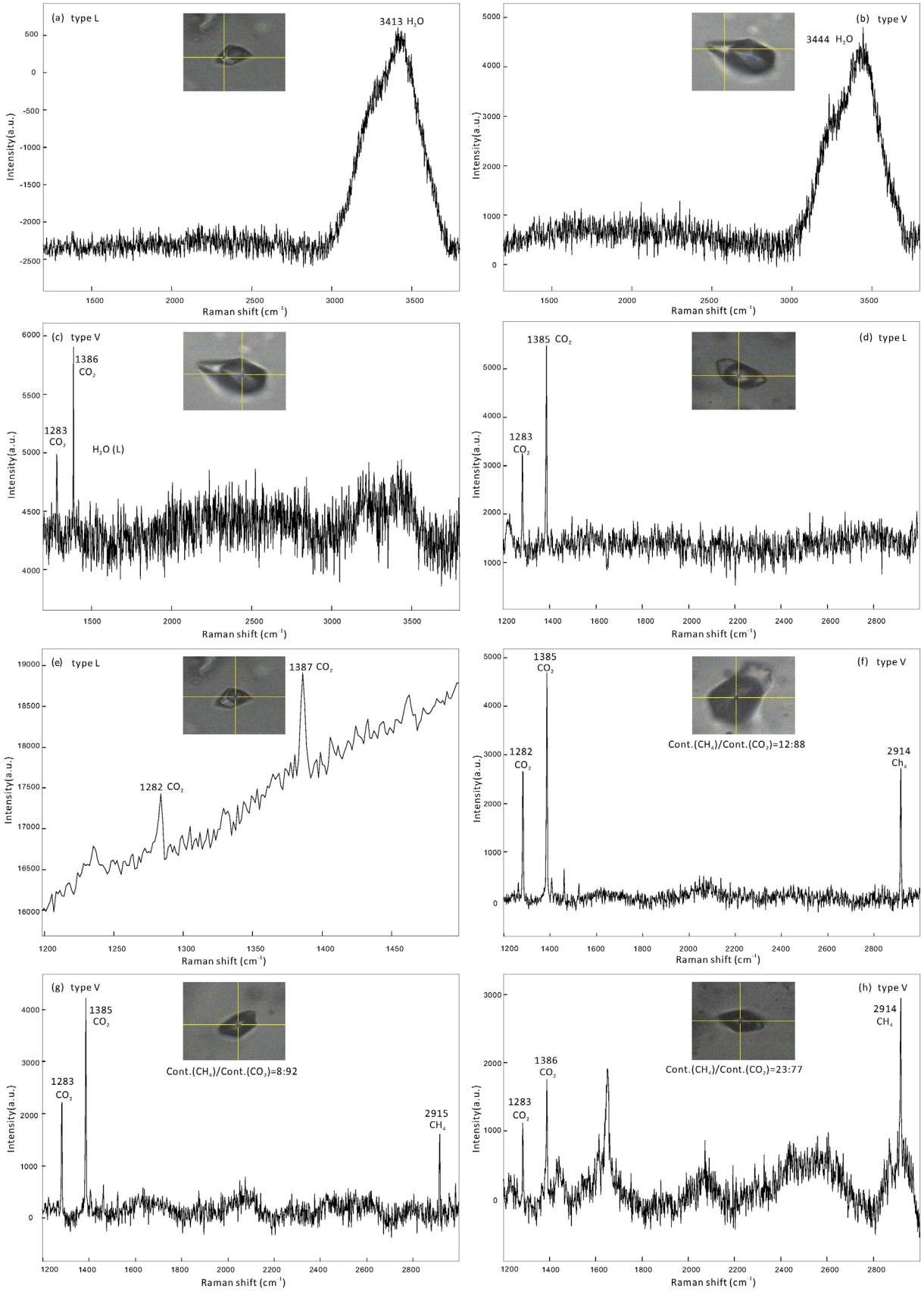

Fig. 14. Laser Raman analyses for type L and V fluid inclusions of quartz at stage III. a. The composition of the liquid phase for type L. b. The composition of the liquid phase for type V. c, f–h. The compositions of the vapor phase for type V. d–e. The compositions of the vapor phase for type L.

Table 3
Summary of sulfur isotope compositions from the Zhibula Cu skarn deposit.

Sample no.	Mineral/rock	Nature	$\delta^{34}S_{V\text{-}CDT}$ (‰)
ZBL1612-78	Chalcopyrite	Chalcopyrite–bornite vein	−4.7
	Bornite		−4.9
Z11-18	Chalcopyrite	Disseminated chalcopyrite and	−4.8
	Molybdenite	molybdenite in green garnet skarn	−3.1
Z11-3	Chalcopyrite	Disseminated chalcopyrite, sphalerite	−5.2
	Sphalerite	and galena in rubricans limestone	−4.3
	Galena		−6.7
Z11-4	Galena	Quartz–galena ± pyrite vein	−4.2
	Sphalerite		−2.8
	Pyrite		−2
Z11-10	Chalcopyrite	Calcite–pyrite–chalcopyrite–bornite vein	−3.5
Z11-26	Chalcopyrite	Disseminated chalcopyrite in dark brown garnet skarn	−4.4
Z11-8	Bornite	Disseminated bornite in green garnet skarn	−6.3
Z11-35	Galena	Chalcopyrite and galena in massive ore	−4.4
ZBL2407-61	Chalcopyrite	Magnetite–chalcopyrite ore	−6.8
ZBL2007-409	Chalcopyrite	Chalcopyrite in quartz vein	−3.1
ZBL2407-#2	Pyrite	Pyrite–calcite vein in tuff	−1.8
ZBL0604-139	Bornite	Disseminated bornite in yellow garnet skarn	−4.1
ZBL0812-247	Molybdenite	Disseminated molybdenite in dark brown garnet skarn	−3.2
ZBL2407-330	Monzogranite		−0.4
ZBL2014-417	Granodiorite		−0.3
ZBL2014-427	Granodiorite		−0.1
ZBL0810-307	Tuff	Rubricans	1.3
ZBL1611-168	Tuff	Rubricans	−4.4
ZBL1611-379	Tuff	Rubricans	−4.2
ZBL1611-182	Marble	Off-white	2.2
ZBL1611-370.5	Marble	Off-white	0.8
QL326*	Sphalerite		−2.5
QL326*	Galena		−3.9
QL318*	Chalcopyrite		−3.7
QL212*	Chalcopyrite		−2.8
QL315*	Pyrite		−0.1

Note: Data of * samples are from She et al. (2005).

Table 4
Hydrogen and oxygen isotope analyses (‰) and the calculated isotope composition of fluids from the Zhibula Cu skarn deposit.

Stage	Sample #	Mineral	δD_{H2O}/‰	$\delta^{18}O_{Mineral}$/‰	Th/°C	$\delta^{18}O_{H2O}$/‰
I	Z11-26	Garnet (red)	−135	5.7	600	9.0
	ZBL1219-428	Garnet (red)	−118	5.6	600	8.9
	ZBL1611-375	Garnet (red)	−129	5.5	600	8.8
	ZBL0804-106	Garnet (yellow)	−128	5.7	600	9.0
	ZBL0804-132.5	Garnet (yellow)	−137	5.4	600	8.7
	Z11-18	Garnet (green)	−159	5.3	600	8.6
	ZBL1219-440	Garnet (green)	−143	5.2	600	8.5
II	ZBL2407-61	Magnetite		2.2	500	9.2
	ZBL0815-307	Magnetite		0.9	500	7.9
III	Z11-6	Quartz	−118	13.9	300	7.0
	Z11-24	Quartz	−107	13.4	327	7.4
	Z11-33	Quartz	−123	12.9	296	5.9
	ZBL2407-60.5	Quartz	−91	10.7	314	4.3
	ZBL1215-348	Quartz	−118	11.2	332	5.4
	ZBL2407-355	Quartz	−107	7.7	320	1.5
	Z11-14	Calcite	−113	9	233	3.0

Notes: The temperatures of garnet, quartz, and calcite were obtained from homogenization temperature measurements of fluid inclusions and the magnetite was inferred from homogenization temperature measurements of fluid inclusions in epidote. The equations used for mineral–water oxygen isotopic fractionation were: $1000\ln\alpha_{magnetite\text{-}H2O} = 2.88 \times 10^6\,T^{-2} - 11.36 \times 10^3\,T^{-1} + 2.89$ (Zheng and Chen, 2000); $1000\ln\alpha_{garnet\text{-}H2O} = 1.22 \times 10^6\,T^{-2} - 4.88$ (Taylor, 1976); $1000\ln\alpha_{quartz\text{-}H2O} = 3.38 \times 10^6\,T^{-2} - 3.40$ (Clayton et al., 1972); $1000\ln\alpha_{calcite\text{-}H2O} = 2.78 \times 10^6\,T^{-2} - 3.39$ (O'Neil et al., 1969).

(Fig. 16a; Taylor, 1974), the majority of the data points are projected under the region of magmatic water, which indicates that the fluid was predominantly magmatic-hydrothermal.

6. Discussion

6.1. Source of the ore-forming material and ore-forming fluids

Sulfur has three different types of $\delta^{34}S$ in nature, including the mantle source of sulfur (0 ± 3‰, Chaussidon and Lorand, 1990), sulfur in seawater (approximately +20‰), and negative strongly reductive sulfur in sediments (almost low to −40‰, Hoefs, 2009). Many researchers claimed that sulfur in skarn deposits was derived from a magmatic origin (e.g., Ault, 2004; Kamvong and Zaw, 2009; Shu et al., 2013), whereas others argued that the sulfur came from mixed sources

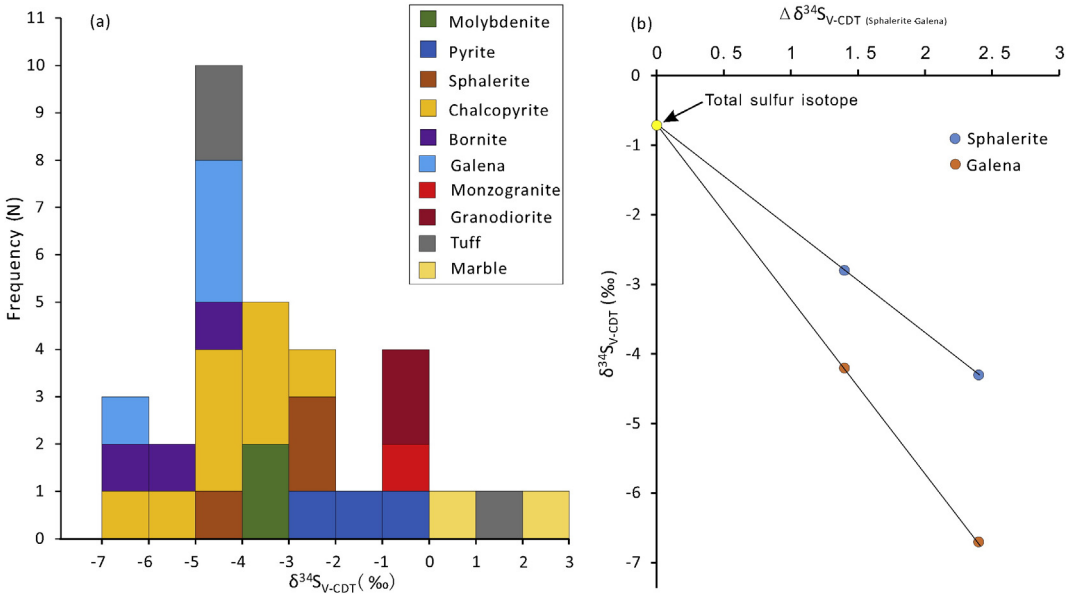

Fig. 15. (a) Frequency histogram plot of $\delta^{34}S_{V\text{-}CDT}$ values; (b) total sulfur estimate by Pinckney and Rafter (1972). The data partly come from She et al. (2005).

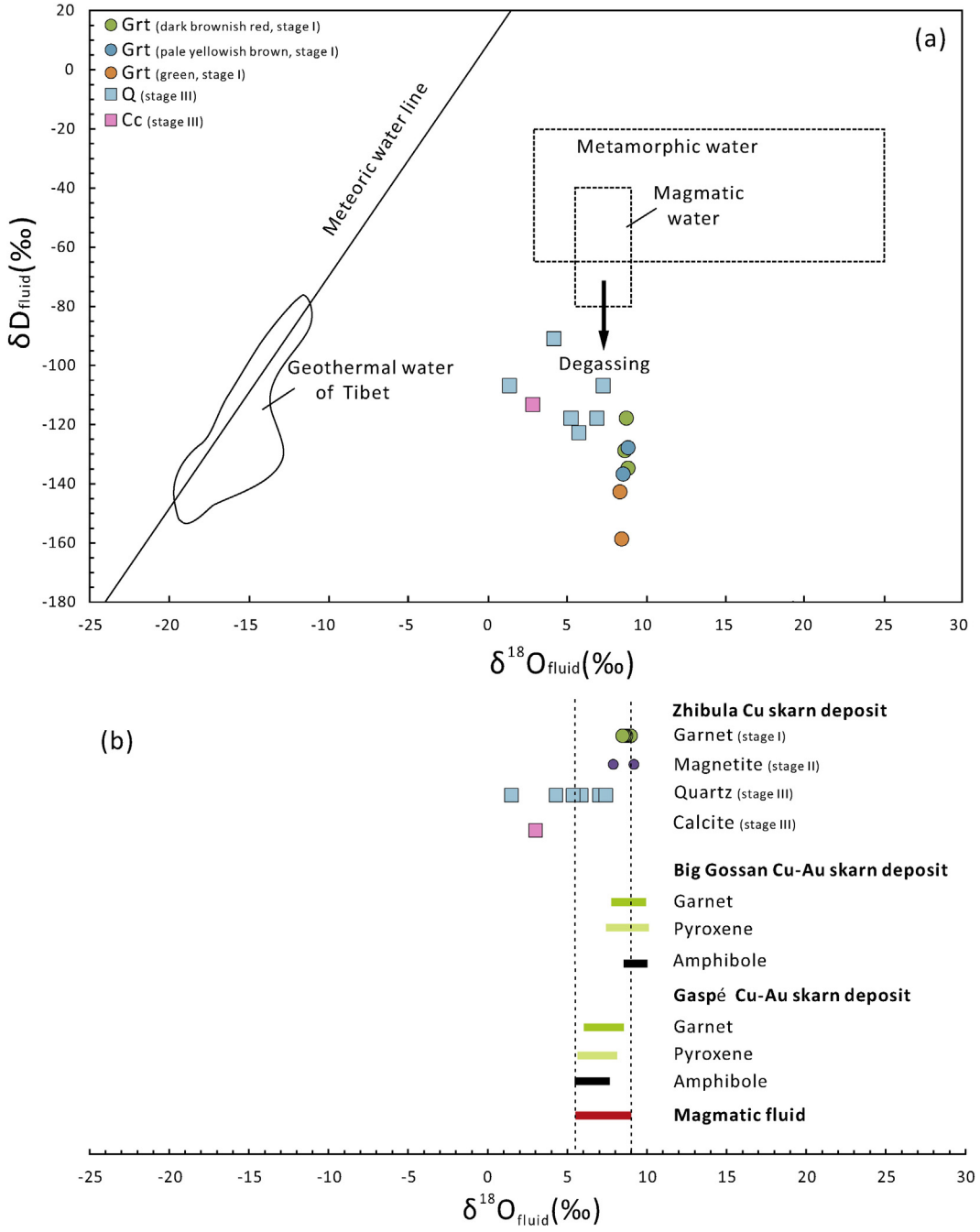

Fig. 16. (a) $\delta^{18}O_{H2O}$ vs. δD_{H2O} diagram of the Zhibula deposit (after Taylor, 1974). (b) The oxygen isotope composition data between the Zhibula deposit and typical skarn deposits worldwide. The oxygen isotope composition data for the Big Gossan and Gaspe skarn deposits are from Meinert et al. (2003).

from magma and host rock (e.g., Ishihara et al., 2000; Zeng et al., 2009). In this study, the $\delta^{34}S_{V\text{-}CDT}$ values of sulfides change in a limited range from −0.1 to −6.8‰ (average − 3.9‰, n = 24), which are analogous to but a slightly more negative than those from mostly magmatic hydrothermal deposits (−3 to +1‰, Hoefs, 2009), and are more limited than those of typical magma-derived fluids (−3 to +7‰, Ohmoto and Goldhaber, 1997). These more negative $\delta^{34}S_{V\text{-}CDT}$ values are probably caused by the processes of magmatic-hydrothermal fluid boiling and degassing (e.g., H_2S; Kamvong and Zaw, 2009; Shu et al., 2013), which is observed in the fluid inclusions at the Zhibula deposit. Paragenetic mineral assemblages (sphalerite and galena) were used to estimate the total sulfur isotopic composition (approximately −0.7‰, Fig. 15b). The values are closer to the $\delta^{34}S$ values of pyrite (average − 1.3‰), which supports that the sulfur isotopic constitution of pyrite can be approximated to the sulfur isotopes of ore-forming fluids under equilibrium conditions (Zheng and Chen, 2000). The total sulfur isotopic composition is extremely similar to the average of the Miocene granodiorite and monzogranite at the Zhibula mine (−0.1 to −0.4‰, average −0.3‰), which indicates that the sulfur originated from Miocene intrusions. In addition, the $\delta^{34}S$ histogram shows a normal distribution, with all the data distributed in a narrow range (concentrated from −3 to −5‰) (Fig. 15a), which suggest that the origin of the sulfur composition is relatively uniform (Ohmoto, 1972). The $\delta^{34}S$ values of the marble vary from +0.8 to +2.2‰ (average + 1.5‰), which excludes the possibility of mixed sulfur sources between intrusion and carbonate rock. However, the influence of tuff cannot be ruled out (−4.4 to

+1.3‰, average − 2.1‰). Summarizing, the ore-forming material was predominantly derived from the Miocene intrusion.

Stable isotope of oxygen and hydrogen have been broadly used to trace the origin and evolution process of hydrothermal fluids with meteoric, magmatic, and metamorphic origins (e.g., Taylor, 1974; Meinert et al., 2003; Lu et al., 2003; Koděra et al., 2010; Soloviev et al., 2013). Einaudi et al. (1981) suggested that two typically distinct alteration styles of skarn ore system from the early prograde stage and later retrograde stage reflect the dominance of magmatic and meteoric water, respectively. Similar researches have been conducted by Bowman (1998) and Koděra et al. (2010). However, Meinert et al. (1997, 2003) argued that both prograde and retrograde alteration can result from the evolution of a single magmatic-hydrothermal system and that is no evidence exists for mixing with a significant component of meteoric water after investigating the Big Gossan Cu–Au skarn deposit. On the δD–$\delta^{18}O_{H2O}$ plot (Fig. 16a), the majority of the data (stage I and stage III) plot close to primary magmatic water region, which indicates that the hydrothermal fluid was probably of magmatic origin. During stage II, the $\delta^{18}O_{H2O}$ values of the magnetite also exhibited primary magmatic water features, ranging from 7.9 to 9.2‰ (5.5–9.0‰; Taylor, 1974). Compared to the $\delta^{18}O_{H2O}$ values of classic skarn deposits worldwide (e.g., the Big Gossan and Gaspe deposits), these data show similarities with magmatic fluids (Fig. 16b; Meinert et al., 2003). Suzuoki and Epstein (1976) and Hedenquist et al. (1998) stated that continuous degassing (e.g., H_2S, CH_4, and HCl) from a crystallizing magmatic source in an open system during the late crystallization stage would decrease the δD content in residual water, whereas the influence of the $\delta^{18}O_{H2O}$ value is less. The lower δD values in the Zhibula deposit indicate that primary magmatic water has been slightly modified by degassing on its pathway the magmatic source to the mineralization site (e.g., De Hoog et al., 2009; Koděra et al., 2010). The lower δD values of the garnet are possibly attributed to the effect of secondary fluid inclusions. Many secondary fluid inclusions that later formed by meteoric water in the garnet were recognized (Fig. 11b), whereas the $\delta^{18}O_{H2O}$ values of the garnet (8.5–9.0‰) were consistent with those of magmatic fluids (Fig. 16b); thus the fluid in the garnet was also derived from magmatic-hydrothermal. In conclusion, the ore-forming fluid had a predominantly magmatic hydrothermal origin.

6.2. Skarn evolution and mineralization

During stage I, the garnet was primarily anhydrous silicate mineral. Pyroxene and minor wollastonite mainly occurred near the off-white marble. Garnet skarns in various colors were the most predominant skarn types (Fig. 8a-c). The homogenization temperatures and salinities of the garnet and pyroxene were 405 to 667 °C and 6.3 to 16.2 wt.% NaCl equiv. (up to 44.0 wt.% NaCl equiv.), respectively. These values agree with classic magmatic hydrothermal fluids with high temperature and high salinity (Chen et al., 2007). Our results are also consistent with Einaudi et al. (1981), who concluded that prograde skarn assemblages generally form at temperatures of 400–650 °C, and Baker et al. (2004), who stated that garnet usually occurs at temperatures of 450–650 °C. Because of fluid immiscibility, the estimated trapping pressures, which were calculated from the formula by Driesner and Heinrich (2007), are mostly between 500 and 600 bar, which corresponds to a depth of approximately 2.1 km according to the lithostatic pressure (Meinert et al., 2003). The prograde assemblages were principally composed of andradite (Fe^{3+}) and diopside (Mg-rich, rather than Fe^{2+}), which indicates that the skarn was oxidized and was produced under low acidity and high oxygen fugacity conditions (Einaudi et al., 1981; Lu et al., 2003; Oyman, 2010). These observations are also confirmed by the hematite and magnetite daughter minerals that are observed in the fluid inclusions in the garnet and pyroxene, respectively (Fig. 11b-d). The absence of a liquid CO_2 phase in these fluid inclusions suggests that the fluid was H_2O-rich and $X_{CO2} < 0.1$ during the prograde stage (e.g., Canet et al., 2011; Soloviev et al., 2013). Chen and Li (2009) considered that this process was probably caused by the reaction between fluids and carbonatite ($CO_2 + H_2O + CaCO_3 = Ca^{2+} + 2HCO_3^-$). Therefore, the evolution process of prograde skarn is as follows. Parental magma was produced at shallow levels (6–8 km) of the crust, and then initial hyperthermal supercritical fluid (6–8 wt.% NaCl equiv.) exsolved from the magma chamber (Meinert et al., 2003). Fournier (1992) claimed that high temperature made the wall rocks behave in a ductile fashion, which prevented mixing with external fluids. As magmatic melt and hydrothermal fluid rose, they intersected its solvus at approximately 2.1 km depth (estimated by the lithostatic pressure) and separated into a hypersaline liquid (44 wt.% NaCl equiv.) and moderate salinity fluid (6.3 to 16.2 wt.% NaCl equiv.) because of the fluid's immiscibility (Fig. 17). Finally, the magmatic fluid produced prograde skarn minerals such as garnet and pyroxene through metasomatic alteration with carbonate rocks. Later in this stage, iron ions reduced in activity and did not participate in the crystal lattice of silicate minerals because of the alkaline nature and high oxygen fugacity; thus iron constituted a separate magnetite. Additionally, magnetite formed by replacing previous garnet (Seward and Barnes, 1997; Maher, 2010) and/or pyroxene (Fig. 6a-c,g).

$$\underset{\text{garnet}}{3Ca_3Fe_2Si_3O_{12}} + 9CO_2 = \underset{\text{calcite}}{9CaCO_3} + \underset{\text{quartz}}{6Ca_2} + \underset{\text{quartz}}{9SiO_2} + 1/2O_2 + \underset{\text{magnetite}}{2Fe_3O_4}$$

During stage II, the temperature of the fluid (402–595 °C) and the trapping pressure (400–600 bar, approximately 1.9 km according to the lithostatic pressure) further decreased, which resulted in fluid immiscibility and phase separation (salinity between 10.2–17.8 and 39.0–50.0 wt.% NaCl equiv.). Strong early retrograde alteration occurred along with increasing hydrolysis (Meinert et al., 2005). In general, prograde skarn was overprinted and replaced by veinlets and vein envelopes of hydrous skarn minerals such as epidote (Berman et al., 1985; Calagari and Hosseinzadeh, 2006; Fig. 6j), actinolite–tremolite (Deer et al., 1992; Fig. 8i), and chlorite.

$$\underset{\text{garnet}}{Ca_3(Fe,\ Al)_2Si_3O_{12}} + 5/4O_2 + HCO_3^- = \underset{\text{calcite}}{CaCO_3} + \underset{\text{epidote}}{Ca_2(Fe,\ Al)_2Si_3O_{12}(OH)} + \underset{\text{hematite}}{1/2Fe_2O_3}$$

$$\underset{\text{pyroxene}}{4Ca(Fe,\ Mg)Si_2O_6} + 2H_2O + 3CO_2 = \underset{\text{tremolite/actinolite}}{Ca_2(Mg,\ Fe)_5Si_8O_{22}(OH)_2} + \underset{\text{calcite}}{CaCO_3} + \underset{\text{quartz}}{2SiO_2}$$

During stage III, the homogenization temperature (194–420 °C, concentrated around 260–340 °C) and trapping pressure (mostly 250–350 bar) greatly reduced (Fig. 13a). The salinities of the ore-forming fluid were 3–15 wt.% NaCl equiv. or 30–42 wt.% NaCl equiv. (Fig. 17). Fluid boiling that was caused by rapidly decreasing of pressure from the activity of several fractures was prominent during this stage in the Zhibula mine (Fig. 2b-c). Fluid boiling separated vapor and liquid phases and produced high salinity, daughter mineral-bearing, and low to moderate salinity and volatile-rich fluids (e.g., CO_2, CH_4; Fig. 14g-i). CH_4 was detected by laser Raman spectroscopy and was reported in many skarn deposits by Fan et al. (2004), Wang et al. (2001), and Zhu et al. (2012). This CH_4 indicates the reducing conditions of the ore-forming fluid. In summary, the ore-forming fluid during the late retrograde stage was moderate-temperature and high-salinity magmatic hydrothermal fluid that was inherited from stage I and stage II and generally belonged to an H_2O – NaCl ± CO_2 ± CH_4 system. During this stage, SiO_2 did not participate in skarn minerals with elements of Ca, Mg, Al, and Fe but precipitated to quartz by crystallization. In general, early skarn minerals partly altered to chlorite, sericite, quartz, and carbonate minerals. The boiling of ore-forming fluids is one of the most crucial mechanisms for the deposition of ore minerals in hydrothermal systems (Wilkinson, 2001; Klemm et al., 2008). Boiling results in broken physical and chemical balances in the original ore-forming fluid system; thus volatiles (CH_4 and CO_2) are separated from ore-forming fluids, which causes the fluid to become concentrated and supersaturated. Bertelli et al. (2009) concluded that neutralization by reactions between acidic ore fluid (pH = 3.9) and limestone will increase the pH, which contributes to

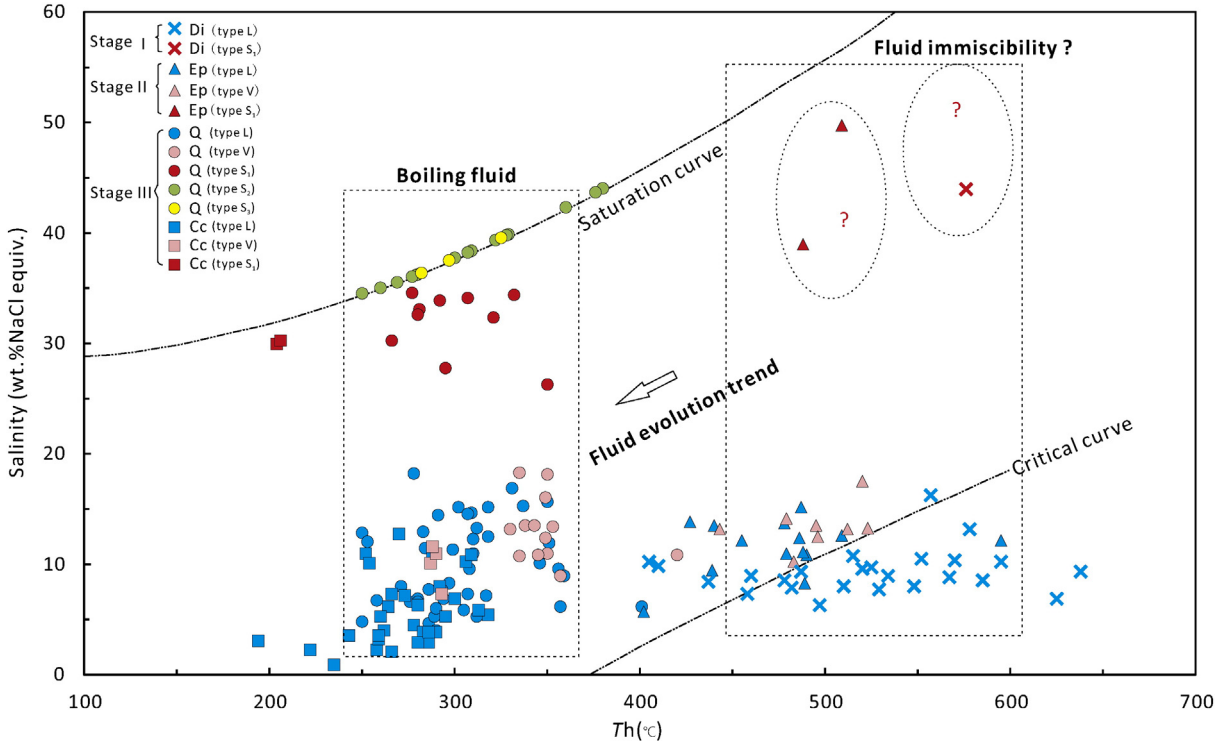

Fig. 17. Fluid evolution of homogenization temperatures and salinities.

ore deposition. In addition, the precipitation of magnetite during the early stage increased Cu/Fe ratios, which changed the sulfur from high valence (S^{6+}, S^{4+}) to reduced valence (S^{2+}) and decreased the Cu solubility in the fluid (Hezarkhani et al., 1999). All these features led to clathrate (e.g., $(CuCl)^0$, $(CuCl_3)^{2-}$, or $(CuCl_3)^{3-}$) dissociation (Bertelli et al., 2009) and sulfide precipitation as disseminated fillings in the interstitial minerals or as quartz–sulfide veins, networks, and veinlet cross-cut the previous skarn.

6.3. Model

The Zhibula Cu orebodies are primarily hosted in interbeds as 'stratiform' and layers between tuff and marble in the Yeba Formation (Fig. 2a,b), which questions whether the Zhibula deposit is a strata-bound skarn deposit that occurred in tuff (e.g., Chang and Liu, 1983) or a sedimentary exhalative skarn deposit (e.g., Lu et al., 1999; Yokoro et al., 2013). In fact, the Zhibula skarn's zonations are similar to those of classic metasomatic skarn deposits that are related to magmatic-hydrothermal fluids (Fig. 4-5; Meinert et al., 1997, 2003, 2005). The orebody of a classic magmatic-hydrothermal skarn deposit can also be stratiform (Nuri W–Mo–Cu skarn deposit, Chen et al., 2012) because of control by interlayer contacts, interlayer fracture zones, and faults. In addition, the Zhibula deposit has neither a particular source bed nor the preliminary enrichment of ore-forming materials (e.g., Chang and Liu, 1983). Zeng et al. (2009) concluded that the ore from the sedimentary exhalative deposit displays fine or particle grain laminar texture. However, the ores from the Zhibula deposit are mostly disseminated, veinlets (Fig. 6a-e), and relic textures. Additionally, the magnetite from the Zhibula deposit exhibits typical features of high temperature and magmatic $\delta^{18}O_{H2O}$ values (Figs. 12c-d, 16b), which are related to the metasomatism of magmatic-hydrothermal fluid.

Moreover, granodiorite and monzogranite were observed in both the Zhibula (drill holes ZK2014 and ZK2007) and Qulong porphyry Cu–Mo deposits (Fig. 2a). Precise in situ zircon SIMS U–Pb ages demonstrated that the geochronology of the granodiorite and monzogranite in the Zhibula deposit (16.9 ± 0.3 Ma and 17.0 ± 0.2 Ma, respectively, unpublished data; 16.0 ± 0.4 Ma, Yao et al., 2015) are consistent with those in the Qulong area (17.4 ± 0.4 Ma, 16.7 ± 0.3 Ma, Zheng et al., 2013). Thus, these deposits are probably deeply interconnected (Li et al., 2005; Xiao et al., 2011; Xu et al., 2014). As seen in the contact between the wall rock and granodiorite (Fig. 4), the granodiorite displays classical endoskarn zonation from the contact to fresh granodiorite, namely a dark red-brown garnet-bearing granodiorite, a green diopside-bearing granodiorite, and a weakly chlorite altered granodiorite (Fig. 4, at depths from 432 to 420.5 m in ZK2014), which is the principal geological evidence that indicates that the intrusion was closely associated with skarn and mineralization. Moreover, Cu skarn mineralization generally occurs in proximal rather than distal intrusions, such as Pb and Zn mineralization (Meinert et al., 2005; Sillitoe, 2010). Combined with the metallogenic age (molybdenite Re–Os 16.90 ± 0.64 Ma) that was recorded by Li et al. (2005), this mineralization is coincident with the timing of the Zhibula intrusion, which indicates that the Zhibula Miocene intrusion was responsible for the formation of the ore. In addition, the sulfur isotopic composition (−0.1‰ to −6.8‰, estimated $\delta^{34}S_{fluids} = -0.7‰$) suggests that the ore-forming material was predominantly derived from the Zhibula intrusion (Fig. 15). The hydrogen (−91‰ to −159‰) and oxygen isotopes (1.5‰ to 9.2‰) and fluid inclusions also originated from high temperature and high salinity magmatic–hydrothermal fluids (Fig. 16). Thus, the Zhibula skarn deposit is associated with Miocene intrusions.

Therefore, the Zhibula Cu skarn deposit is a typical metasomatic stratiform skarn deposit of magmatic-hydrothermal origin, whose metallogenic model is as follows (Fig. 18). The ore-bearing magmatic hydrothermal fluids, under the drive of temperature and pressure from magma, were channeled in interbeds along the lithologic interface or in fracture zones. Then, skarns were formed by selective metasomatism between tuff or marble and hydrothermal fluids during the prograde stage. During the retrograde stage, the temperature, salinity, and pressure of the fluid gradually reduced, whereas the reducibility and pH of the fluid increased. The boiling of ore-forming fluids lead to clathrate dissociation and sulfide precipitation (Bertelli et al., 2009).

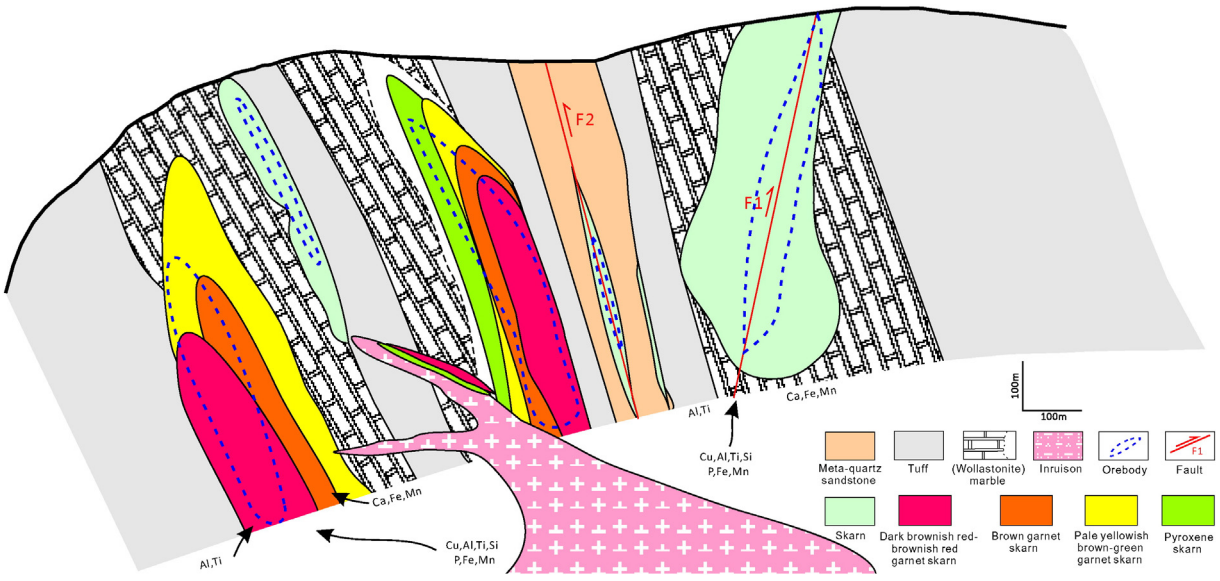

Fig. 18. Schematic illustration showing the genetic model for the Zhibula Cu skarn deposit.

7. Conclusions

(1) The Zhibula Cu skarn deposit is a metasomatic stratiform skarn deposit that is related to magmatic-hydrothermal processes. The endoskarn grades from a fresh granodiorite into a weakly chlorite-altered granodiorite, a green diopside-bearing granodiorite, and a dark red-brown garnet-bearing granodiorite. The exoskarn mostly occurs in the interlayer between tuff and marble and exhibits classic zonation. Andradite and diopside predominantly occur at the prograde stage, which indicates relatively oxidizing conditions.

(2) The types of fluid inclusions include type L, type V, and type S. As the skarn formation stage evolved from prograde (stage I) to early retrograde (stage II) and later retrograde (stage III), ore-forming fluids evolved from high temperature, high salinity, and high pressure to low-moderate temperature, moderate-high salinity, and low-moderate pressure.

(3) The temperatures that were derived from isotope geothermometry are in good agreement with the determined fluid inclusion trapping temperatures and indicate that ore formation occurred between 278 and 449 °C.

(4) Fluid inclusion, sulfur, hydrogen, and oxygen studies showed that ore-forming materials and fluids originated from a magmatic-hydrothermal environment with high temperature and high salinity. Fluid boiling is likely the most crucial mechanism of the sulfide mineral deposition.

Conflict of interest

We declare that we do not have any commercial or associative interest that represents a conflict of interest in connection with the work submitted.

Acknowledgments

We are deeply grateful to the anonymous reviewer for the constructive comments and suggestions. We also thank Dr. Franco Pirajno for his editorial handling. Research for this paper was supported by the Commonweal Project from the Ministry of Land and Resources (201511015), Changjiang Scholars and Innovative Research Team in University (IRT14R56, IRT1083), China Geological Survey (1212011220927, 12120114039701), Specialized Research Fund for the Doctoral Program of Higher Education, National Natural Science Foundation of China (Grant No. 41302063), Fundamental Research Funds for the Central Universities, and Beijing Higher Education Young Elite Teacher Project.

References

Atkinson, W.W., Einaudi, M.T., 1978. Skarn formation and mineralization in the contact Aureole at Carr Fork, Bingham, Utah. Econ. Geol. 73 (7), 1326–1365.
Audétat, A., Günther, D., 1999. Mobility and H_2O loss from fluid inclusions in natural quartz crystals. Contrib. Mineral. Petrol. 137, 1–14.
Ault, K.M., 2004. Sulfur and lead isotope study of the El Mochito Zn–Pb–Ag deposit. Econ. Geol. 99 (6), 1223–1231.
Baker, T., Lang, J.R., 2003. Reconciling fluid inclusion types, fluid processes, and fluid sources in skarns: an example from the Bismark Deposit, Mexico. Mineral. Deposita 38 (4), 474–495.
Baker, T., Van Achterberg, E., Ryan, C.G., Lang, J.R., 2004. Composition and evolution of ore fluids in a magmatic–hydrothermal skarn deposit. Geology 32 (2), 117–120.
Becker, S.P., Fall, A., Bodnar, R.J., 2008. Synthetic fluid inclusions. XVII. PVTX properties of high salinity H_2O–NaCl solutions (>30 wt.% NaCl): application to fluid inclusions that homogenize by halite disappearance from porphyry copper and other hydrothermal ore deposits. Econ. Geol. 103, 539–554.
Berman, R.G., Brown, T.H., Greenwood, H.J., 1985. Heat capacity of minerals in the system Na_2O–K_2O–CaO–MgO–FeO–Fe_2O_3–Al_2O_3–SiO_2–TiO–H_2O–O_2. Contrib. Mineral. Petrol. 89 (2–3), 168–183.
Bertelli, M., Baker, T., Cleverley, J.S., Ulrich, T., 2009. Geochemical modelling of a Zn–Pb skarn: constraints from LA-ICP-MS analysis of fluid inclusions. J. Geochem. Explor. 102 (1), 13–26.
Bodnar, R.J., 1993. Revised equation and table for determining the freezing point depression of H_2O–NaCl solutions. Geochim. Cosmochim. Acta 57, 683–684.
Bowman, J.R., 1998. Stable-isotope systematics of skarns. Mineral. Assoc. Can. Short Course 26, 99–145.
Brown, P.E., Hagemann, S.G., 1995. MacFlinCor and its application to fluids in Archean lode-gold deposits. Geochim. Cosmochim. Acta 59 (19), 3943–3952.
Burke, E.A.J., 2001. Raman microspectrometry of fluid inclusions. Lithos 55 (1–4), 139–158.
Calagari, A.A., Hosseinzadeh, G., 2006. The mineralogy of copper-bearing skarn to the east of the Sungun-Chay River, East-Azarbaidjan, Iran. J. Asian Earth Sci. 28 (4), 423–438.
Canet, C., González-Partida, E., Camprubí, A., Castro-Mora, J., Romero, F.M., Prol-Ledesma, R.M., Linares, C., Romero-Guadarrama, J.A., Sánchez-Vargas, L.I., 2011. The Zn–Pb–Ag skarns of Zacatepec, Northeastern Oaxaca, Mexico: a study of mineral assemblages and ore-forming fluids. Ore Geol. Rev. 39 (4), 277–290.
Chang, I.F., Liu, X.G., 1983. On strata-bound skarn deposites. Mineral. Deposita 2 (1), 11–20 (in Chinese with English abstract).
Chang, Z.S., Meinert, L.D., 2004. The magmatic–hydrothermal transition-evidence from quartz phenocryst textures and endoskarn abundance in Cu–Zn skarns at the Empire mine, Idaho, USA. Chem. Geol. 210 (1–4), 149–171.
Chaussidon, M., Lorand, J.P., 1990. Sulphur isotope composition of orogenic spinel lherzolite massifs from Ariege (North-Eastern Pyrenees, France): an ion microprobe study. Geochim. Cosmochim. Acta 54 (10), 2835–2846.

Chen, Y.J., Li, N., 2009. Nature of ore-fluids of intercontinental intrusion-related hypothermal deposits and its difference from those in island arcs. Acta Petrol. Sin. 25 (10), 2477–2580.

Chen, Y.J., Chen, H.Y., Zaw, K., Pirajno, F., Zhang, Z.J., 2007. Geodynamic settings and tectonic model of skarn gold deposits in China: an overview. Ore Geol. Rev. 31, 139–169.

Chen, L., Qin, K., Li, J., Xiao, B., Li, G., Zhao, J., Fan, X., 2012. Fluid inclusions and hydrogen, oxygen, sulfur isotopes of Nuri Cu–W–Mo deposit in the southern Gangdese, Tibet. Resour. Geol. 62 (1), 42–62.

Chung, S.L., Liu, D.Y., Ji, J.Q., Chu, M.F., Lee, H.Y., Wen, D.J., Lo, C.H., Lee, T.Y., Qian, Q., Zhang, Q., 2003. Adakites from continental collision zones: melting of thickened lower crust beneath southern Tibet. Geology 31 (11), 1021–1024.

Clayton, W.M., Mayeda, T.K., 1963. The use of bromine pent a fluoride in the extraction of oxygen from oxides and silicates for isotopic analysis. Geochim. Cosmochim. Acta 27, 43–52.

Clayton, R.N., O'Neil, J.R., Mayeda, T.K., 1972. Oxygen isotope exchange between quartz and water. J. Geophys. Res. 77, 3057–3067.

Cline, J.S., Bodnar, R.J., 1994. Direct evolution of brine from a crystallizing silicic melt at the Questa, New Mexico, molybdenum deposit. Econ. Geol. 89, 1780–1802.

Coleman, M.L., Sheppard, T.J., Durham, J.J., Rouse, J.E., Moore, G.R., 1982. Reduction of water with zinc for hydrogen isotope analysis. Anal. Chem. 54, 993–995.

De Hoog, J., Taylor, B.E., Van Bergen, M.J., 2009. Hydrogen-isotope systematics in degassing basaltic magma and application to Indonesian arc basalts. Chem. Geol. 266 (3), 256–266.

Deer, W.A., Howie, R.A., Zussman, J., 1992. An Introduction to the Rock-Forming Minerals. Longman Group Ltd., New York, pp. 1–696 (Prentice Hall, England).

Deng, J., Wang, Q.F., Li, G.J., Li, C.S., Wang, C.M., 2014. Tethys tectonic evolution and its bearing on the distribution of important mineral deposits in the Sanjiang region. SW China. Gondwana Res. 26, 419–437.

Driesner, T., Heinrich, C.A., 2007. The system H_2O–NaCl. Part I: correlation formulae for phase relations in temperature-pressure-composition space from 0 to 1000 °C, 0 to 5000 bar, and 0 to 1 X_{NaCl}. Geochim. Cosmochim. Acta 71, 4880–4901.

Droop, G.T.R., 1987. A general equation for estimating Fe3+ concentrations in ferromagnesian silicates and oxides from microprobe analyses, using stoichiometric criteria. Mineral. Mag. 51, 431–435.

Einaudi, M.T., Meinert, L.D., Newberry, R.J., 1981. Skarn deposits. Econ. Geol. 75th anniversary volume, 317–391.

Fan, H.R., Xie, Y.H., Wang, K.Y., Wilde, S.A., 2004. Methane-rich fluid inclusions in skarn near the giant REE-Nb-Fe deposit at Bayan Obo, northern China. Ore Geol. Rev. 25 (3), 301–309.

Fournier, R.O., 1992. The influences of depth of burial and the brittle-ductile transition on the evolution of magmatic fluids. Geol. Surv. Jpn. Rep. 277, 57–59.

Gemmell, J.B., Zantop, H., Meinert, L.D., 1992. Genesis of the Aguilar zinc-lead-silver deposit, Argentina; contact metasomatic vs. sedimentary exhalative. Econ. Geol. 87 (8), 2085–2112.

Geng, Q.R., Pan, T.G., Jin, Z.M., Wang, L.Q., Zhu, D.C., Liao, Z.L., 2005. Geochemistry and genesis of the Yeba volcanic rocks in the Gangdese magmatic arc, Tibet. Earth Sci. 30 (6), 747–760 (in Chinese with English abstract).

Harris, N.B., Einaudi, M.T., 1982. Skarn deposits in the Yerington district, Nevada; metasomatic skarn evolution near Ludwig. Econ. Geol. 77 (4), 877–898.

Hedenquist, J.W., Reyes, A.G., Simmons, S.F., Taguchi, S., 1992. The thermal and geochemical structure of geothermal and epithermal systems: a framework for interpreting fluid inclusion data. Eur. J. Mineral. 4, 989–1015.

Hedenquist, J.W., Arribas, A., Reynolds, T.J., 1998. Evolution of an intrusion-centered hydrothermal system; far Southeast-Lepanto porphyry and epithermal Cu-Au deposits, Philippines. Econ. Geol. 93 (4), 373–404.

Hezarkhani, A., Williams-Jones, A.E., Gammons, C.H., 1999. Factors controlling copper solubility and chalcopyrite deposition in the Sungun porphyry copper deposit, Iran. Mineral. Deposita 34 (8), 770–783.

Hoefs, J., 2009. Stable Isotope Geochemistry. 6th ed. Springer-Verlag, Berlin Heidelberg, p. 285.

Hou, Z.Q., Zhang, H.R., Pan, X.F., Yang, Z.M., 2011. Porphyry Cu (−Mo–Au) deposits related to melting of thickened mafic lower crust: examples from the eastern Tethyan metallogenic domain. Ore Geol. Rev. 39, 21–45.

Ishihara, S., Jin, M.S., Sasaki, A., 2000. Source diversity of ore sulfur from Mesozoic–Cenozoic Miner. Deposits in the Korean peninsula region. Resour. Geol. 50, 203–212.

Jamtveit, B., 1991. Oscillatory zonation patterns in hydrothermal grossular-andradite garnet; nonlinear dynamics in regions of immiscibility. Am. Mineral. 76 (7–8), 1319–1327.

Kamvong, T., Zaw, K., 2009. The origin and evolution of skarn-forming fluids from the Phu Lon deposit, northern Loei Fold Belt, Thailand: evidence from fluid inclusion and sulfur isotope studies. J. Asian Earth Sci. 34 (5), 624–633.

Klemm, L.M., Pettke, T., Heinrich, C.A., 2008. Fluid and source magma evolution of the Questa porphyry Mo deposit, New Mexico, USA. Mineral. Deposita 43, 533–552.

Koděra, P., Lexa, J., Fallick, A.E., 2010. Formation of the Vysoká-Zlatno Cu–Au skarn–porphyry deposit, Slovakia. Mineral. Deposita 45 (8), 817–843.

Li, G.M., Rui, Z.Y., Wang, G.M., Lin, F.C., Liu, B., She, H.Q., Feng, C.Y., Qu, W.J., 2005. Molybdenite Re–Os dating of Jiama and Zhibula polymetallic copper deposits in Gangdese metallogenic belt of Tibet and its significance. Mineral. Deposita 24 (5), 481–489 (in Chinese with English abstract).

Li, G.M., Li, F.Q., Duan, Z.M., 2012. The assessment report of geology and mineral resources survey in Gangdese metallogenic belt, Tibet (in Chinese, unpublished).

Lu, Y.F., Chen, K.X., Zhan, M.G., 1999. Geochemical evidence of Exhalative-Sedimentary ore-bearing Skarn Yangla copper mineralization concentrated area, Deqin County, Northwestern Yunman Province. Earth Sci. 24 (3), 298–303 (in Chinese with English abstract).

Lu, H.Z., Liu, Y., Wang, C., Xu, Y., Li, H., 2003. Mineralization and fluid inclusion study of the Shizhuyuan W–Sn–Bi–Mo–F skarn deposit, Hunan Province, China. Econ. Geol. 98 (5), 955–974.

Maher, K.C., 2010. Skarn alteration and Mineralization at Coroccohuayco, Tintaya District, Peru. Econ. Geol. 105 (2), 263–283.

Mei, W., Lü, X., Cao, X., Liu, Z., Zhao, Y., Ai, Z., Abfaua, M.M., 2014. Ore genesis and hydrothermal evolution of the Huanggang skarn iron–tin polymetallic deposit, southern Great Xing'an Range: evidence from fluid inclusions and isotope analyses. Ore Geol. Rev. 64, 239–252.

Meinert, L.D., Hefton, K.K., Mayes, D., Tasiran, I., 1997. Geology, zonation, and fluid evolution of the Big Gossan Cu–Au skarn deposit, Ertsberg district, Irian Jaya. Econ. Geol. 92 (5), 509–534.

Meinert, L.D., Hedenquist, J.W., Satoh, H., Matsuhisa, Y., 2003. Formation of anhydrous and hydrous skarn in Cu–Au ore deposits by magmatic fluids. Econ. Geol. 98 (1), 147–156.

Meinert, L.D., Dipple, G.M., Nicolescu, S., 2005. World skarn deposits. Econ. Geol. ^{100}th anniversary volume, 299–336.

Ohmoto, H., 1972. Systematics of sulfur and carbon isotopes in hydrothermal ore deposits. Econ. Geol. 67 (5), 551–578.

Ohmoto, H., Goldhaber, M.B., 1997. Sulfur and carbon isotopes. In: Barnes, H.L. (Ed.), Geochemistry of hydrothermal ore deposits, 3rd ed. Wiley, New York, pp. 517–611.

Ohmoto, H., Rye, R.O., 1979. Isotopes of sulfur and carbon. In: Barnes, H.L. (Ed.), Geochemistry of hydrothermal ore deposits, 2nd ed. Wiley-Interscience, New York, pp. 509–567.

O'Neil, J.R., Clayton, R.N., Meyada, T.K., 1969. Oxygen isotope fracdonation in divalent metal carbonates. J. Chem. Phys. 51, 5547–5558.

Oyman, T., 2010. Geochemistry, mineralogy and genesis of the Ayazmant Fe–Cu skarn deposit in Ayvalik, (Balikesir), Turkey. Ore Geol. Rev. 37 (3), 175–201.

Pinckney, D.M., Rafter, T.A., 1972. Fractionation of sulfur isotopes during ore deposition in the Upper Mississippi Valley zinc–lead district. Econ. Geol. 67 (3), 315–328.

Robinson, B.W., Kusabe, M., 1975. Quantitative preparation of sulphur dioxide for $^{34}S/^{32}S$ analyses from sulphides by combustion with cuprous oxide. Anal. Chem. 47, 1179–1181.

Roedder, E., Bodnar, R.J., 1980. Geologic pressure determinations from fluid inclusion studies. Annu. Rev. Earth Planet. Sci. 8, 263–301.

Samson, I.M., Williams-Jones, A.E., Ault, K.M., Gagnon, J.E., Fryer, B.J., 2008. Source of fluids forming distal Zn–Pb–Ag skarns: evidence from laser ablation-inductively coupled plasma-mass spectrometry analysis of fluid inclusions from El Mochito, Honduras. Geology 36 (12), 947–950.

Seward, T.M., Barnes, H.L., 1997. Metal Transport by Hydrothermal Ore Fluids. Geochem. Hydrotherm. Ore Deposits 3, 435–486.

She, H.Q., Feng, C.Y., Zhang, D.Q., Pan, G.T., Li, G.M., 2005. Characteristics and metallogenetic potential of skarn copper–lead–zinc polymetallic deposits in central eastern Gangdese. Mineral. Deposita 24 (5), 508–552 (in Chinese with English abstract).

Shepherd, T.J., Rankin, A.H., Alderton, D.H.M., 1985. A Practical Guide to Fluid Inclusion Studies. Blackie and Sons Ltd., Glasgow, p. 239.

Shu, Q.H., Lai, Y., Sun, Y., Wang, C., Meng, S., 2013. Ore genesis and hydrothermal evolution of the Baiyinnuo'er zinc-lead skarn deposit, northeast China: evidence from isotopes (S, Pb) and fluid inclusions. Econ. Geol. 108 (4), 835–860.

Sillitoe, R.H., 2010. Porphyry copper systems. Econ. Geol. 105, 3–41.

Singoyi, B., Zaw, K., 2001. A petrological and fluid inclusion study of magnetite-scheelite skarn mineralization at Kara, Northwestern Tasmania: implications for ore genesis. Chem. Geol. 173 (1), 239–253.

Smith, M.P., Henderson, P., Jeffries, T.E.R., 2004. The rare earth elements and uranium in garnets from the Beinn an Dubhaich Aureole, Skye, Scotland, UK: constraints on processes in a dynamic hydrothermal system. J. Petrol. 45 (3), 457–484.

Soloviev, S.G., Kryazhev, S.G., Dvurechenskaya, S.S., 2013. Geology, mineralization, stable isotope geochemistry, and fluid inclusion characteristics of the Novogodnee-Monto oxidized Au–(Cu) skarn and porphyry deposit, Polar Ural, Russia. Mineral. Deposita 48 (5), 603–627.

Sterner, S.M., Hall, D.L., Bodnar, R.J., 1988. Synthetic fluid inclusions.V. Solubility relations in the system NaCl–KCl–H_2O under vapor-saturated conditions. Geochim. Cosmochim. Acta 52, 989–1006.

Sun, X., Zheng, Y.Y., Wang, C.M., Zhao, Z.Y., Geng, X.B., 2016. Identifying geochemical anomalies associated with Sb–Au–Pb–Zn–Ag mineralization in North Himalaya, southern Tibet. Ore Geol. Rev. 73, 1–12.

Sun, X., Zheng, Y.Y., Wu, S., Li, M., Ouyang, H.T., Geng, R.R., 2013. Mafic enclaves at Jiru porphyry Cu deposit, southern Tibet: implication for the Eocene magmatichydrothermal Cu mineralization. Acta Geol. Sin. (Engl. Ed.) 87, 778–782.

Suzuoki, T., Epstein, S., 1976. Hydrogen isotope fractionation between O–H-bearing minerals and water. Geochim. Cosmochim. Acta 40 (10), 1229–1240.

Tang, J.X., Deng, S.L., Zheng, W.B., Ying, L.J., Wang, X.W., Zhong, K.H., Qin, Z.P., Ding, F., Li, F.J., Tang, X.Q., Zhong, Y.F., Peng, H.J., 2011. An exploration model for Jiama copper polymetallic deposit in Maizhokunggar County, Tibet. Mineral. Deposita 32 (2), 179–196 (in Chinese with English abstract).

Taylor Jr., H.P., 1974. The application of oxygen and hydrogen isotope studies to problems of hydrothermal alteration and ore deposition. Econ. Geol. 69 (6), 843–883.

Taylor, B.E., 1976. Origin and significance of C–O–H fluids in the fomation of Ca–Fe–Si skam, Osgood Mountains, Humboldt County, Nevada. Unpublished PhD thesis, Stanford University. 306.

Törnebohm, A.E., 1875. Geognostisk Beskrifning of ver Persbergets Grufvefält. Sveriges Geologiska Undersökning. Norstedt and Sons, Stockholm, P.A., p. 21.

Vallance, J., Fontboté, L., Chiaradia, M., Markowski, A., Schmidt, S., Vennemann, T., 2009. Magmatic-dominated fluid evolution in the Jurassic Nambija gold skarn deposits (southeastern Ecuador). Mineral. Deposita 44, 389–413.

Van den Kerkhof, A.M., Hein, U.F., 2001. Fluid inclusion petrography. Lithos 55 (1), 27–47.
Wang, L.J., Hidehiko, S., Wang, J., Wang, Y., 2001. Ore-forming fluid and metallization of the Huangangliang skarn Fe–Sn deposit, Inner Mongolia. Sci. China Ser. D Earth Sci. 44 (8), 735–747.
Wilkinson, J.J., 2001. Fluid inclusions in hydrothermal ore deposits. Lithos 55 (1), 229–272.
Wilkinson, J.J., Crowther, H.L., Coles, B.J., 2011. Chemical mass transfer during hydrothermal alteration of controls of seafloor subsidence, sedimentation and Zn–Pb mineralization in the Irish Carboniferous. Chem. Geol. 289 (1), 55–75.
Williams-Jones, A.E., Samson, I.M., Ault, K.M., Gagnon, J.E., Fryer, B.J., 2010. The genesis of distal zinc skarns: Evidence from the Mochito deposit, Honduras. Econ. Geol. 105 (8), 1411–1440.
Wu, Y.C., 1992. On magmatic skarn-a new type of skarn. Geol. Anhui 2 (1), 12–26 (in Chinese with English abstract).
Wu, S., Zheng, Y., Sun, X., 2016. Subduction metasomatism and collision-related metamorphic dehydration controls on the fertility of porphyry copper ore-forming high Sr/Y magma in Tibet. Ore Geol. Rev. 73, 83–103.
Xiao, B., Qin, K.Z., Ling, G.M., Li, J.X., Chen, L., Zhao, J.X., Fan, X., 2011. Distributions and characters of Zhibula-Langmujiaguo skarn Cu deposits environing the Qulong porphyry Cu-Mo deposit and their implications for ore-search towards to the deep subsurface. Geol. Explor. 47 (1), 43–53 (in Chinese with English abstract).
Xu, J., Zheng, Y.Y., Sun, X., Jiang, J.S., Geng, R.R., Shen, Y.H., 2014. Mineral characteristics in the Zhibula skarn Cu deposit of Tibet and their geological significance. Earth Sci. 39, 654–670 (in Chinese with English abstract).
Yao, X.F., Tang, J.X., Ding, S., Zheng, W.B., Yang, H.H., Zhang, W.Y., Feng, Y.F., 2015. Petrography, chronology and Hf isotope constraints on origin of the ore-bearing granodiorite in Zhibula copper deposit, Tibet. Geotecton. Metallog. 39 (2), 315–324 (in Chinese with English abstract).
Yin, A., Harrison, T.M., 2000. Geologic evolution of the Himalayan–Tibetan orogen. Annu. Rev. Earth Planet. Sci. 28 (1), 211–280.
Yokoro, Y., Hanamuro, T., Nakashima, K., 2013. Unique origin of skarn at the Ohori base metal deposit, Yamagata Prefecture, NE Japan: C, O and S Isotopic Study. Resour. Geol. 63 (4), 384–393.
Zeng, Q.D., Liu, J.M., Zhang, Z.L., Jia, C.S., Yu, C.M., Ye, J., Liu, H.T., 2009. Geology and lead isotope study of the Baiyinnuo'er Zn–Pb–Ag deposit, south segment of the Da Hinggan Mountains, northeastern China. Resour. Geol. 59, 170–180.
Zhai, D.G., Liu, J.J., Zhang, H., Yao, M., Wang, J., Yang, Y., 2014. S–Pb isotopic geochemistry, U–Pb and Re–Os geochronology of the Huangangliang Fe–Sn deposit, Inner Mongolia, NE China. Ore Geol. Rev. 59, 109–122.
Zhang, D.H., Xu, G.J., Zhang, W.H., Golding, S.D., 2007. High salinity fluid inclusions in the Yinshan polymetallic deposit from the Le-De metallogenic belt in Jiangxi Provice, China: their origin and implications for ore genesis. Ore Geol. Rev. 31, 247–260.
Zhang, Z.Y., Du, Y.S., Zhang, J., 2013. Alteration, mineralization, and genesis of the zoned Tongshan skarn-type copper deposit, Anhui, China. Ore Geol. Rev. 53, 489–501.
Zheng, Y.F., Chen, J.F., 2000. Stable isotope geochemistry 10. Sci. Press, Beijing, p. 12.
Zheng, Y.Y., Xie, Y.X., Cheng, L.J., Fan, Z.H., Gao, S.B., 2004. Finding, characteristics and significances of Qulong super-large porphyry copper (molybdenum) deposit, Tibet. Earth Sci. 29 (1), 103–108 (in Chinese with English abstract).
Zheng, Y.Y., Sun, X., Gao, S.B., 2013. Qulong super large porphyry copper molybdenum deposit in Tibet. Geol. Pub. House, Beijing (in Chinese).
Zheng, Y.Y., Sun, X., Gao, S.B., Zhao, Z.D., Zhang, G.Y., Wu, S., You, Z.M., Li, J.D., 2014. Multiple mineralization events at the Jiru porphyry copper deposit, southern Tibet: implications for Eocene and Miocene magma sources and resource potential. J. Asian Earth Sci. 9 (Part B), 842–857.
Zheng, Y.Y., Sun, X., Gao, S.B., Wu, S., Xu, J., Jiang, J.S., Chen, X., Zhao, Z.Y., Liu, Y., 2015. Metallogenesis and the minerogenetic series in the Gangdese polymetallic copper belt. J. Asian Earth Sci. 103, 23–39.
Zhu, M., Wu, G., Xie, H., Liu, J., Mei, M., 2012. Geochronology and fluid inclusion studies of the Lailisigaoer and Lamasu porphyry–skarn Cu–Mo deposits in Northwestern Tianshan, China. J. Asian Earth Sci. 49, 116–130.